

UNIVERSIDADE DE SÃO PAULO
INSTITUTO DE ASTRONOMIA, GEOFÍSICA E CIÊNCIAS
ATMOSFÉRICAS
DEPARTAMENTO DE GEOFÍSICA

PLINIO FRANCISCO JAQUETO

Magnetism of a speleothem from Midwest Brazil and paleoclimatic
implications

Magnetismo de um espeleotema do Centro-Oeste do Brasil e suas implicações
paleoclimáticas

São Paulo

2016

PLINIO FRANCISCO JAQUETO

Magnetism of a speleothem from Midwest Brazil and paleoclimatic
implications

Magnetismo de um espeleotema do Centro-Oeste do Brasil e suas implicações
paleoclimáticas

Dissertação apresentada ao Departamento de
Geofísica do Instituto de Astronomia,
Geofísica e Ciências Atmosféricas da
Universidade de São Paulo como requisito
para a obtenção do título de Mestre em
Ciências.

Área de Concentração: Geofísica
Orientador: Prof. Dr. Ricardo Ivan Ferreira da
Trindade

São Paulo

2016

to my grandparents

Acknowledgements

I would like to say thanks to my advisor prof. Ricardo Ivan Ferreira da Trindade for the support, help and friendship in all these years, they were fundamental to achieve the results. He always has been an enthusiastic of speleothem magnetism, and provides so many good opportunities.

This research could only happen because of the professors Francisco William da Cruz Jr. (Chico Bill) and Ivo Karmann from Instituto de Geociências, which always encourage and discuss with me the study of speleothem and provided many samples for me. Also, Valdir, Nicolás, Jean-Sebastien and Fernando helped a lot in field trips, analysis and support to this research.

I thank to IRM at University of Minnesota for the Visiting Research Fellowship, specially Mike Jackson, Pete Solheid, Becky Strauss and prof. Joshua Feinberg that helped in all discussions and provided substantial help to my research.

Prof. Joe Kirschvink from Caltech allowed me to learn a lot about rock magnetism and superconducting rock magnetometer in his lab, always showing how exciting the geological materials can be.

I thank CAPES for continuous support through scholarships along these years.

I'm very grateful for IAG Staff: Wellington, Miguel, Márcio, Reginaldo, Roberto, Eliza, Virgínia, Teca, Lilian and professors.

USPMag is definitely the best lab in the world!! This could only happen because of the people that are there, especially Daniele, Wilbor, Grasiene, Karine, Gelvam, Janine, Aruã, Rafael (Cabelo), Giovanni, Sônia, Elder, Filipe, Mari, Thiago, Oscar, Genérico, Anita and everyone that the names I can't remember (feel included here).

Charlie's friends are the best, Chocolate, Fernando (Loko), Mori, Angélica, Danilo, Adriana, Diana, Fábio, Núria and Estela thanks for everything. Also, Yadyr, Renatinho, Priscila, Ale (Espanhol), Kid Vinil, Rapha, Caio, Marcão, Ivan thanks for all the laughs and support.

My parents have always been an inspiration to me, you've given me freedom to become what I am, and for this I will always be grateful. Also, the supports of all my parents made me move forward to do this.

Love makes me move forward, you have inspired me, supported me and teach me so many things, thanks for everything.

“Life swings like a pendulum backward and forward between pain and boredom”.

Arthur Schopenhauer

Resumo

Jaqueto, P. F. **Magnetismo de um espeleotema do Centro-Oeste do Brasil e suas implicações paleoclimáticas**. 2016. 84 pp. Dissertação (Mestrado) – Instituto de Astronomia, Geofísica e Ciências Atmosféricas, Universidade de São Paulo, São Paulo, 2016.

Esta tese fornece um estudo detalhado do magnetismo ambiental de espeleotemas. Este estudo é feito em uma estalagmite da caverna Pau D'Alho (15 ° 12'20 "S, 56 ° 48'41" W), localizado em Rosário d'Oeste, Mato Grosso, Brasil. Este espeleotema cresceu durante os últimos 1355 anos, com taxa média de crescimento de ~ 168 mm/ka e engloba dois eventos climáticos do Sistema de Monção Sul-americano (SMSA), a Anomalia Climática do Medieval (ACM) e a Pequena Idade do Gelo (PIG), eventos secos e molhados, respectivamente. Os experimentos de magnetismo de rocha incluem: magnetização remanente isothermal (MRI), ciclos de histerese, magnetização remanente anisterética (MRA), desmagnetização térmica em três eixos, *first order reversal curves* (FORC) e experimentos de baixa temperatura. Os principais portadores magnéticos na estalagmite são magnetita e goethita, com uma proporção relativa quase constante. A magnetita tem coercividades entre 14-17 mT, e as suas propriedades magnéticas são semelhantes às produzidas por processos pedogênicos. As remanências magnéticas são amplamente correlacionadas com dados de isótopos de carbono e oxigênio durante o registro, sugerindo que a precipitação e a dinâmica do solo acima da caverna exerce um forte controle na entrada de minerais magnéticos no sistema de cavernas Pau d'Alho. Períodos secos como o ACM estão associados a solos menos estáveis, que resultam em maiores fluxos de minerais detríticos carregados para o sistema de cavernas, ao passo que, inversamente, os períodos frios e chuvosos como a LIA estão associados a solos cobertos pela vegetação mais densa que são mais capazes de reter minerais pedogênicos de escala micrométrica, e, assim, diminuir os fluxos de minerais detríticos para o sistema de cavernas.

Palavras chave: magnetismo de espeleotema, magnetismo de rochas, solo, paleoclima, magnetismo ambiental.

Abstract

Jaqueto, P. F. **Magnetism of a speleothem from Midwest Brazil and paleoclimatic implications.** 2016. 84 pp. Thesis (Master's degree) – Departamento de Geofísica, Instituto de Astronomia, Geofísica e Ciências Atmosféricas, Universidade de São Paulo, São Paulo, 2016.

This thesis provides a detailed study of environmental magnetism in a speleothem. It focuses on a stalagmite from Pau D'Alho cave (15°12'20"S, 56°48'41"W) located in Rosário d'Oeste, Mato Grosso State, Brazil. This speleothem grew during the past 1355 years, with average growth rate of ~168 mm/ka and encompasses two key events in the South American Summer Monsoon (SASM), the Medieval Climate Anomaly (MCA) and the Little Ice Age (LIA), major dry and wet, respectively. The rock magnetic experiments conducted, include isothermal remanent magnetization (IRM) and anhysteretic remanent magnetization (ARM) acquisition curves, thermal demagnetization of three-axis IRM acquisition, hysteresis loops, first order reversal curves (FORC) and low-temperature SQUID magnetometry experiments. The main magnetic remanence carriers in the stalagmite are magnetite and goethite, with a nearly constant relative proportion. Magnetite has remanent coercivities between 14-17 mT, and its magnetic properties are similar to those produced by pedogenic processes. Magnetic remanence is broadly correlated with carbon and oxygen isotope data throughout most of the speleothem, suggesting that precipitation and soil dynamics above the cave exert a strong control on the input of magnetic minerals into the Pau d'Alho cave system. Dry periods like the MCA are associated with less stable soils that result in higher mineral fluxes carried into karst systems via groundwater, while conversely, colder and wetter periods like the LIA are associated with soils topped by denser vegetation that are more capable of retaining micrometer-scale pedogenic minerals, and thus reduce mineral fluxes into karst environments.

Keywords: speleothem magnetism, rock magnetism, soil, paleoclimate, environmental magnetism.

Summary

| | |
|--|----|
| Chapter 1: Introduction | 1 |
| Chapter 2: Isotope records and magnetism of speleothems and soils | 4 |
| 2.1 The karst system..... | 4 |
| 2.2 Oxygen isotopes in speleothems | 6 |
| 2.3 Carbon isotopes in speleothems | 9 |
| 2.4 Speleothem magnetism | 13 |
| 2.5 Soil magnetism..... | 19 |
| Chapter 3: Theoretical background of environmental magnetism | 23 |
| 3.1 Rock magnetic measurements and environmental magnetic significance | 23 |
| Chapter 4: Methods | 32 |
| 4.1 Sample preparation..... | 32 |
| 4.2 Remanence measurements | 34 |
| 4.3 Low temperature experiments on bulk rock and magnetic extracts | 37 |
| Chapter 5: Results | 38 |
| 5.1. Age of the Alho 6 stalagmite..... | 38 |
| 5.2 Oxygen and Carbon Isotope records | 39 |
| 5.2 Hysteresis and FORC diagrams | 41 |
| 5.3 ARM acquisition curves and Cisowski test..... | 44 |
| 5.4 IRM acquisition curves and Lowrie test..... | 47 |
| 5.5 Unmixing methods and remanence ratios | 49 |
| 5.6 Low-temperature SQUID magnetometry (FC-ZFC, RTSIRM)..... | 54 |
| Chapter 6: Discussion | 57 |
| 6.1 The source of magnetic minerals | 57 |
| 6.2 Variation in the magnetic signal and paleoclimatic significance | 59 |
| Chapter 7: Conclusion and Perspectives | 65 |
| References | 66 |
| Appendix 1 | 72 |

Chapter 1: Introduction

The word 'speleothem' has its origin from the Greek *spelaiion* (cave) and *thema* (deposit). These geological materials are secondary deposits formed by chemical precipitation in karstic environments (Gornitz, 2009), being usually composed of calcite and/or aragonite (CaCO_3). Essentially, calcium carbonate is dissolved in the soil and in the upper epikarst, and is precipitated in the underlying vadose region. As the water descends through the karst, it ultimately encounters a gas phase with a lower $p\text{CO}_2$. This causes degassing of CO_2 from the solution and precipitation of CaCO_3 forming structures that serve as continuous archives for paleoclimatic studies. Over the last decades, speleothems have become an important record for studies of climate change, due to their long and continuous nature and their potential to preserve orbital, millennial, decadal, annual, or even sub-annual processes (Wong & Breecker, 2015). In recent years, the rapid advance in analytical techniques improved the sensibility and accuracy of equipments that enable us to make multiple measurements in one single record, allowing the study of diverse environmental indicators in a single speleothem (Fairchild & Baker, 2012).

The magnetic study of speleothems started with Latham (1979). The focus of the first studies was to obtain the directional data of the Earth's magnetic field. The challenges at the time involved two main factors: (1) obtain a good dating model, using techniques such as ^{14}C and ^{230}Th (Alfred G Latham, Schwarcz, Ford, & Pearce, 1979; Martin, 1990) that at the time presented large uncertainties, (2) detection of the magnetic signal due to the low concentration of magnetic minerals in these geological samples (Lascu & Feinberg, 2011). The size of samples for ^{230}Th dating changed from few tens of grams in the 1980s to milligrams in recent years, achieving good analytical precision to as low as 1% (Fairchild & Baker, 2012) providing nowadays a good age control for the continuous age models necessary for paleoclimatic studies (Cheng et al., 2013). At the same time, the evolution of Superconducting Rock Magnetometers (SRM) such as the 2G enterprises system allowed sensitivity in magnetic moment detection in the order of magnitude of 10^{-12}Am^2 . The new generation of u-channel magnetometers allows the measurement of continuous sections and

specimens with spatial resolution of 5 mm (Jackson, Bowles, Lascu, & Solheid, 2010). Combining the major advances in ^{230}Th dating, magnetometer technology and the environmental magnetism research, speleothem magnetism has experienced a revival in the past years (e.g., Lascu & Feinberg, 2011; Font et al., 2014; Bourne et al., 2015). Recent studies in the field are not limited to the study of the Earth's magnetic field, but use the magnetic speleothem record as a tool for high resolution reconstruction of regional climate, erosion or pedogenic histories.

In this present dissertation, the magnetic study of a stalagmite from the cave Pau D'Alho (15°12'20"S, 56°48'41"W) located in Rosário d'Oeste, Mato Grosso State, Brazil, is presented. The main focus is the origin of the magnetic minerals and their relation with climate and vegetation in a karst system. The stalagmite was previously studied by Novello et al. (2016), who presented an age model based on ^{230}Th dating and a detailed record of $\delta^{18}\text{O}$ and $\delta^{13}\text{C}$. This stalagmite covers two distinct climate periods in Midwest Brazil, a drier period (Medieval Climatic Anomaly) that occurred between ~900 years CE¹ to ~1100 years CE and a wet period (Little Ice Age) that occurred between ~1600 years CE to ~1820 years CE (Novello et al., 2016). The objective of the magnetic study is to understand the magnetic mineral signal present in the stalagmite, and the meaning of this signal. Magnetic experiments used a sensitive rock magnetometer (Superconducting Rock Magnetometer), thermomagnetic curves, FORC diagrams, and scanning electron microscope images.

The dissertation is structured in six chapters including this Introduction (Chapter 1). Chapter 2 discusses the processes involved in stalagmite formation and the meaning of its $\delta^{18}\text{O}$ and $\delta^{13}\text{C}$ isotopic composition, in particular the influence of climate, soil and vegetation composition on the isotope signal. Speleothem magnetism is then reviewed in order to establish the major advances in the field since the first studies. Environmental magnetism with a particular focus on soil magnetism is also discussed in this chapter. Chapter 3 concerns the methods and presents details of sample preparation and magnetic techniques used in the present work. Chapter 4 presents the results obtained and correlations between them. Chapter 5 summarizes key results and presents a discussion on the origin of magnetic minerals found in the Pau d'Alho stalagmite, variations in their

¹ Common Era is abbreviated as C.E, and it refers as the same as Anno Domini (AD).

concentration throughout the speleothem and their interpretation in face of the oxygen and carbon isotopic records. In Chapter 6 the conclusions are presented and a framework for future studies to assess the magnetic minerals of stalagmites is presented.

Chapter 2: Isotope records and magnetism of speleothems and soils

2.1 The karst system

Klimchouk & Ford, (2000) offer the following definition for the karst system, “*It is an integrated mass-transfer system in soluble rocks with permeability structure dominated by conduits dissolved from the rock and organized to facilitate the circulation of fluid*”. The dynamics of the karst involves surface environments such as climate, soil and vegetation. So, speleothems are part of a long history of cave space building (Fairchild & Baker, 2012). In carbonate rocks, the rainfall is acidified with carbon dioxide (CO₂) present in the atmosphere and undergoes enrichment in carbonic acid when passes through the soil, as a result of plant respiration and organic matter dissolution along the upper epikarst (high fissured) zone. The underlying vadose region (water table) is the location where the precipitation of CaCO₃ occurs (Figure 2.1). The precipitation region corresponds to the carbonate supersaturation zone. Speleothem precipitation is induced by degassing of CO₂ from descending waters into cave’s fissure porosity.

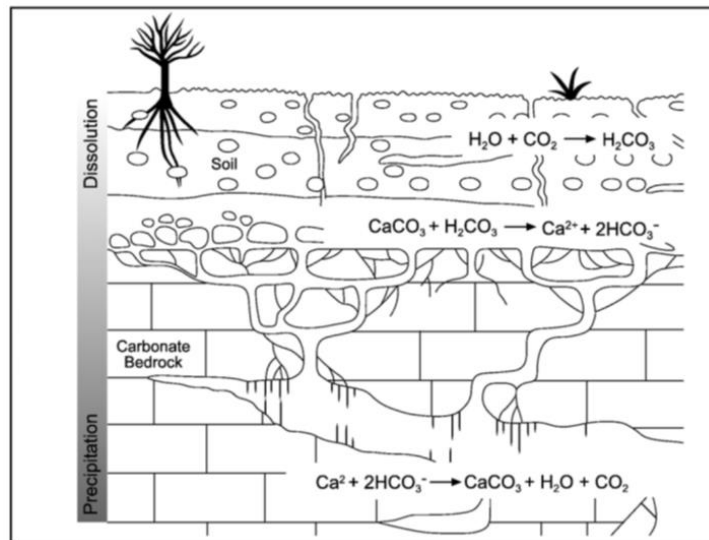


Figure 2.1: Dissolution and precipitation zones involved on the formation of a speleothem (extracted from Fairchild et al. 2006).

The climatic component determines the input of water in the karst system. Climate also influences strongly vegetation (chemistry of the carbonate system) and soil properties (facilitating speleogenesis) (Fairchild et al., 2006). A stalagmite (CaCO_3) precipitates from water moving gravitationally and it originated from drip water; this record through time is an excellent archive for the changes that occurred in the hydrological dynamics above and inside the cave. Historically, much of the research on speleothems dealt with the disequilibrium in uranium series isotopes to determine the age of the material, using the age models to constrain the oxygen isotope time series is an attempt to elucidate paleotemperature variations (Fairchild & Baker, 2012). The use of oxygen isotopes as a paleoclimate proxy has begun in the 1960's. It represents the main continental record, together with lake data, that complements the record obtained in marine sediment cores. Cave environments are stable and their isotopic record reflects the regional mean temperature (Lachniet, 2009). Rapid advances in analytical techniques in the last decade opened the possibility that a single speleothem can provide a combined dataset with time series of $\delta^{18}\text{O}$, $\delta^{13}\text{C}$, trace elements, speleothem growth-rates and organic matter fluorescence properties (Cruz et al., 2006).

2.2 Oxygen isotopes in speleothems

Oxygen is the second most abundant gas (O₂) in the atmosphere. It occurs in nature as three isotopes, the lighter ¹⁶O accounts for almost 99.76% of the total, ¹⁷O corresponds to only 0.04% and the heavier ¹⁸O accounts for 0.2%. Individual measurements of the ¹⁸O/¹⁶O ratio in natural materials are reported as departures in parts per mil (‰) from the value of a standard:

$$\delta^{18}\text{O}_{(in\text{‰})} = \frac{(\text{}^{18}\text{O}/\text{}^{16}\text{O})_{\text{sample}} - (\text{}^{18}\text{O}/\text{}^{16}\text{O})_{\text{standard}}}{(\text{}^{18}\text{O}/\text{}^{16}\text{O})_{\text{standard}}} \times 1000 \quad [2.1]$$

where samples with positive $\delta^{18}\text{O}$ values are said to be enriched in ¹⁸O (compared to ¹⁶O) and samples with negative $\delta^{18}\text{O}$ values are said to be ¹⁸O depleted. The heavier the oxygen isotope the more rapidly it is removed from the atmosphere when condensation and precipitation occur. Repeated cycles of evaporation and precipitation through time leave the water vapor progressively more enriched in ¹⁶O (Ruddiman, 2001).

The study of oxygen isotopes ($\delta^{18}\text{O}$) time series in Brazil started in the southern region, which is a well-situated location for investigating the changes in tropical and subtropical atmospheric circulation (Cruz et al., 2005). Stalagmite isotope record in combination with ²³⁰Th age model of the Botuverá cave provided a record of the intensity variation of the South America Summer Monsoon and enabled its correlation with the insolation controlled by orbital forcing (Figure 2.2). The authors called attention to the progressive increase in humidity during the Holocene, besides dry periods around 60, 40 and between 23 and 11 kyrs. Another important aspect of that work was the identification of an antiphase relationship between the South America Summer Monsoon and the Asian Monsoon, attributed to the latitudinal position of the Intertropical Convergence Zone during the summer insolation. In tropical and subtropical areas of South America the “amount effect” on interannual timescales leads to more depleted $\delta^{18}\text{O}$ values in rainfall in wet years and relatively more enriched $\delta^{18}\text{O}$ values during dry years.

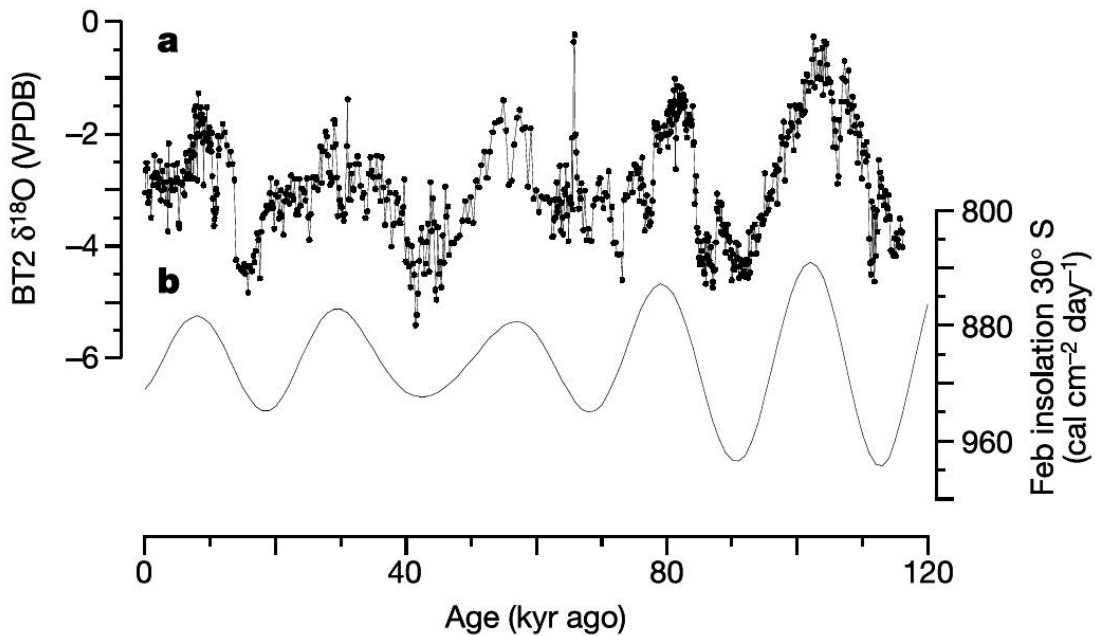


Figure 2.2: Relation between oxygen isotope record of Botuverá cave and insolation from February on latitude 30°. (Modified from Cruz et al., 2005)

Studies of the South American monsoon for the past millennia (Vuille et al. 2012, and references therein) combined high-resolution oxygen isotope measurements with cave monitoring and climate modeling to address the variations in the South America Summer Monsoon (SASM) intensity. Collectively, these studies show that the stalagmite oxygen isotope record is a robust regional proxy for paleoprecipitation and paleoclimate monitoring. The monsoon belt in tropical Andes and SE Brazil along the past ~2000 years is characterized by significant decadal to multidecadal variability superimposed to large excursions during three key periods: the Medieval Climate Anomaly (MCA) between ~900 and ~1100 CE, the Little Ice Age (LIA), between ~1600 and ~1820 CE and the Current Warm Period (CWP), corresponding to the last ~100 years. The SASM was significantly weakened during MCA and CWP and strengthened during LIA (Vuille et al., 2012).

More recently, Novello et al. (2016) used a high-resolution paleoclimate record based on $\delta^{18}\text{O}$ in the Alho 6 stalagmite, located at the core of the South American Monsoon System (SAMS), to detail how solar variability consistently modulated the strength of the SAMS on centennial time scales during the last ~1500 years. The periodicity of 208-years is

persistent in the whole record and the in-phase relationship between the speleothem record and a reconstruction of total solar irradiance indicates once more that tropical precipitation is strongly sensitive to solar forcing.

2.3 Carbon isotopes in speleothems

Two nonradioactive isotopes of carbon occur in nature, the ^{12}C that accounts for more than 98.89%, and the ^{13}C that comprises the remaining 1.11%. Individual measurements of the $^{13}\text{C}/^{12}\text{C}$ ratio in natural materials are reported as departures in parts per mil (‰) from the standard:

$$\delta^{13}\text{C}_{(in\text{ ‰})} = \frac{(^{13}\text{C}/^{12}\text{C})_{sample} - (^{13}\text{C}/^{12}\text{C})_{standard}}{(^{13}\text{C}/^{12}\text{C})_{standard}} \times 1000 \quad [2.2]$$

where samples with positive $\delta^{13}\text{C}$ values are said to be enriched in ^{13}C (compared to ^{12}C) and samples with negative $\delta^{13}\text{C}$ values are said to be ^{13}C depleted. Carbon isotope ratios can be measured in a wide range of materials such as speleothems, bones, leaves, shells, carbonates, soils, sediments, peats and wood, the isotopic variation being linked to climate effects on the global carbon cycle and photosynthetic pathways of plants (Figure 2.3) (Gornitz, 2009). All trees as well as most shrubs use a type of photosynthesis called the C_3 pathway, which produces organic tissues with more negative $\delta^{13}\text{C}$ values when compared to some shrubs and most grasses that use a different kind of photosynthesis called C_4 pathway.

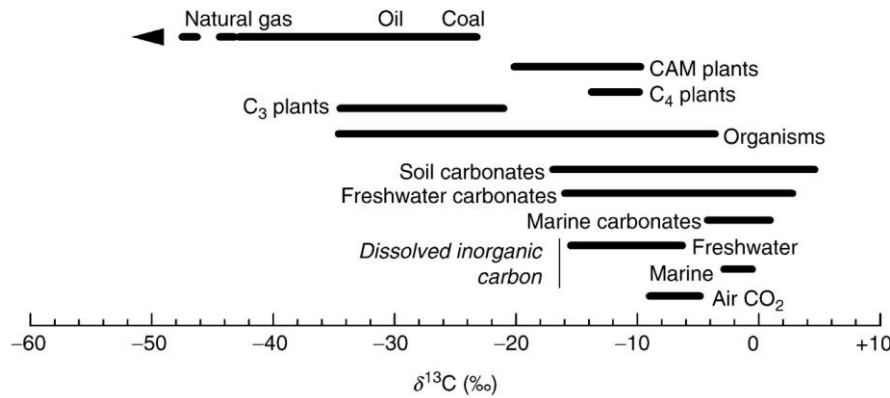


Figure 2.3: Typical values from carbon isotope of natural materials (Gornitz, 2009).

The carbon isotope signal recorded by a speleothem is controlled by processes occurring mainly in the soil/epikarst and inside the cave (Fairchild & Baker, 2012; Wong and Breecker, 2015), but the interpretation of $\delta^{13}\text{C}$ signal is variable and often region/case specific, including: the $\delta^{13}\text{C}$ value of atmospheric carbon dioxide, the proportions of C_3/C_4 vegetation, the soil/vegetation productivity controlled by precipitation and temperature, carbon isotope fractionation during decomposition of soil organic matter, the proportion of host rock carbon, and in-cave precipitation (e.g. ventilation, prior calcite precipitation)(Boch, Spötl, & Frisia, 2011; Breitenbach et al., 2015; Meyer, Feng, Breecker, Banner, & Guilfoyle, 2014; Spötl, Fairchild, & Tooth, 2005). In soils, water availability can also control the magnitude of photosynthetic discrimination, where drier and/or hotter climate (higher evaporation and lower soil water content) results in less negative organic carbon values (Wong & Breecker, 2015). The control of rapid biomass shifts in the soil over the cave on the carbon isotope signal of stalagmites can be exemplified by the case study conducted by Baldini et al. 2005). These authors reported an increase in calcite deposition rates in the karst system coeval with a decrease in $\delta^{13}\text{C}$ and $\delta^{18}\text{O}$ in a well-documented re-vegetation area of an abandoned mine. According to those authors, this signal reveals that the $\delta^{13}\text{C}$ data is able to record vegetation shifts, and suggests that the $\delta^{13}\text{C}$ variation may partly result from changes in the amount of biomass as well as to the shifts in the distribution of C_3/C_4 plant species.

In Brazil, Cruz et al. (2005) presented a 116 ka carbon stable isotope record from the Botuverá stalagmite, with the aim of investigating the effect of changes in large-scale atmospheric circulation on the temperature-driven biological activity and soil CO₂ productivity during the last glaciation. It was found that the most important determinant of carbon isotope variation is the change in the amount of CO₂ input to the soil waters. The main controls on this parameter are the processes that occur above the cave, such as the rate of organic matter decomposition and the type of vegetation cover. Greater soil CO₂ production results in a greater fraction of the isotopically-depleted soil source being incorporated into the stalagmite. Conversely, when soil CO₂ production is smaller the relatively enriched limestone source of the epikarst is privileged. The fact that more negative $\delta^{13}\text{C}$ intervals in the Botuverá stalagmite were also those with higher growth rates (Figure 2.4) supports this idea.

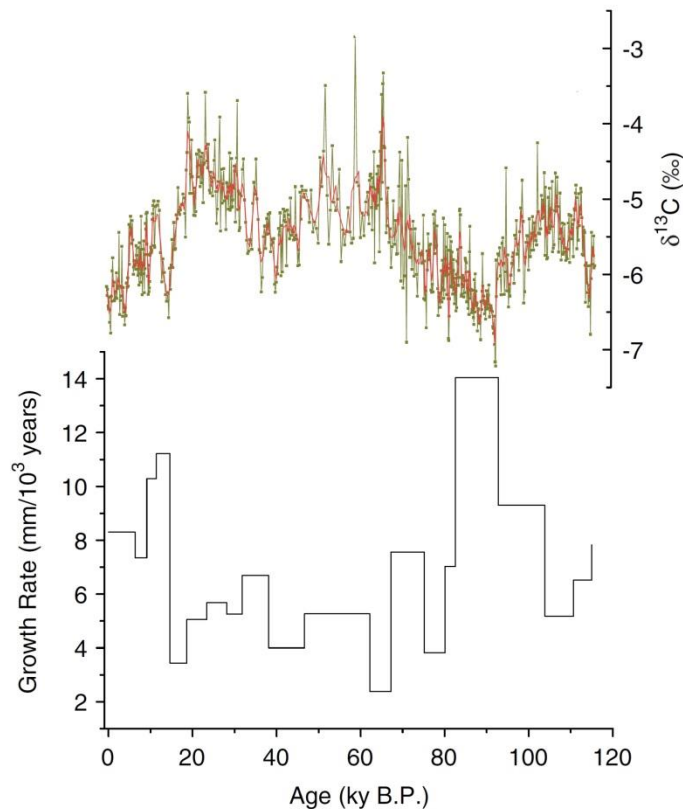


Figure 2.4: Stable carbon isotope and growth rates from stalagmite BT2 (Botuverá Cave), from Southern Brazil (Modified from Cruz et al., 2005)

Changes in $\delta^{13}\text{C}$ in soils of tropical Brazil are usually driven by changes in the relative contributions of C_3 and C_4 plant communities to the carbon isotope composition of soil organic matter (SOM) (Pessenda, Gouveia, Ribeiro, De Oliveira, & Aravena, 2010). During wetter intervals, as denser forests (C_3 plants) replace savanna grasslands (C_4 plants), soils display a decrease in the $\delta^{13}\text{C}$ of their SOM. The increase in soil biomass during forest expansion is also likely to generate a higher concentration of isotopically lighter biogenic carbon, regardless of the relative ratio of C_3 and C_4 plants (Baldini et al., 2005).

2.4 Speleothem magnetism

The first studies of speleothem magnetism focused on the paleosecular variation (PSV) of the Earth's Magnetic Field (EMF) (Latham et al. 1979; Latham 1981; Latham et al. 1989; Morinaga et al. 1986; Morinaga 1989; Morinaga et al. 1992; Martin 1990; Openshaw et al., 1997), because these geological objects provide continuous and instantaneous records of the EMF direction, being thus an alternative to other magnetic archives such as lake sediments and volcanic rocks.

The research that first demonstrated speleothem magnetism as a potential recorder of the EMF was made by Latham et al. (1979). The authors used stalagmites and flowstones from Canada and United Kingdom. From nine samples collected only five were used due to the low concentration of magnetic minerals and viscous instabilities. The best result (Figure 2.5) shows a continuous variation of the EMF from 12.5 to 10 kyrs. The magnetic mineral identified in the stalagmites through demagnetization curves was magnetite. Despite the large uncertainty in the ages this research established the future directions for speleothem magnetism research until the 1990's.

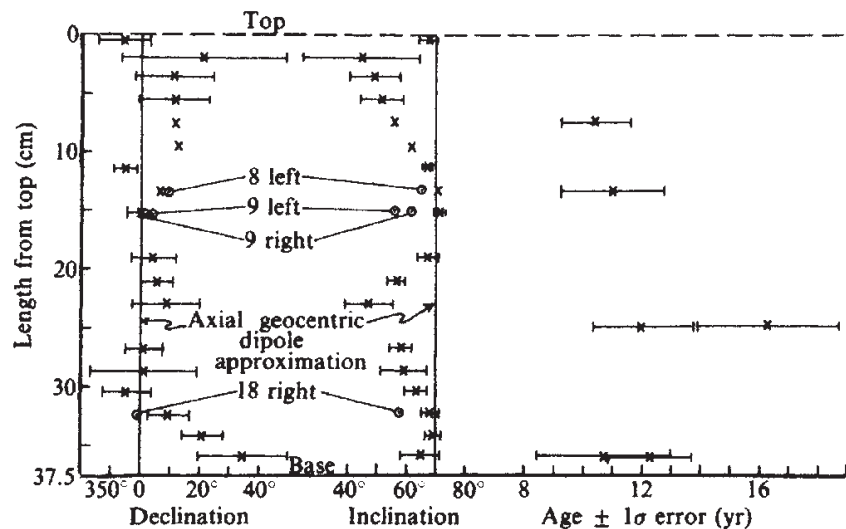


Figure 2.5: First recorded published of speleothem magnetism, the line at declination and inclination is referred to the location $D=8^\circ$ and $I=69^\circ$ (extracted from Latham et al., 1979).

Morinaga et al. (1986, 1989, and 1992) studied stalagmites from western Japan. The magnetic carrier determined was again magnetite, through studies of Isothermal Remanent

Magnetization (IRM) curves and thermomagnetic curves. Although Morinaga and his coauthors did not have access to a dating method (Morinaga et al., 1986, 1989), it was possible to compare the speleothem data with available archaeomagnetic curves for the last 2000 years in Southwest Japan. This is the first study to relate the dominant magnetic mineral found in the stalagmites to that observed on the overlying soils and sediments, in their case the soils and sediments exposed in the Akioishi Plateau (Morinaga et al., 1986). The authors suggested that the magnetic mineral (magnetite) has been deposited after being carried either as a detrital grain or in solution within the dripping water into the cave, the magnetization being acquired at the time of crystallization of the stalagmite.

Finally, in the 1990's, some studies of speleothem magnetism were consecrated to the origin of speleothem remanence (e.g. Perkins & Maher, 1993; Perkins, 1996; Openshaw et al., 1997). The potential of speleothems as recorders of PSV has been successfully demonstrated before, but the origins for the speleothem magnetism were not well documented. Perkins & Maher (1993) listed the advantages of using speleothems as a recorder of the EMF : (1) the remanence acquisition time – the remanence of the top of active speleothems were close to the EMF at the cave location indicating that acquisition time-lag is negligible; (2) sedimentary problems – speleothems are not subject to compaction or slumping, and dissolution or gaps in the record can be easily identified in the laminae; (3) the low intensity of their natural remanent magnetization is a problem, but a careful choice of samples can solve it; (4) diagenetic problems – the only diagenetic problem is the occurrence of recrystallization, that is easily detectable in thin section by crystallographic changes; (5) biological problems – biogenically derived magnetite could overprint a sedimentary remanence, but no organisms are known to burrow into subaerial speleothems; (6) sampling problems – no disturbances occur with collecting speleothems because they are solid rocks, and the sample can be oriented *in-situ*; (7) dating problems – fluid movements caused by sedimentary processes and bioturbation in sediments can lead to incorrect radiocarbon dates, whereas in speleothems these processes do not occur, their dating being made by ^{230}Th techniques (eventual contamination with detrital thorium can be corrected). This work also demonstrates that two stalagmites from the same cave reproduce the magnetic record of contemporaneous deposits of lake sediments (Figure 2.6). Extraction of magnetic minerals was carried by Perkins (1996) for electron microscopy and energy

dispersive X-ray analyses. Three major groups were identified: (1) detrital grains composed of magnetite, hematite and titanomagnetite; (2) unabraded grains composed of magnetite, with two possible origins (bacterial magnetite from the overlying soil or inorganic authigenic magnetite precipitated in the cave); (3) needle-like grains, probably composed of goethite. The last research that appeared in 1990's was made by Openshaw et al. (1997), where five stalagmites from China were used to investigate the paleosecular variation. The comparison between the speleothem record and the modern field suggested a westward drift of non-dipole sources during the last 2.8 kyrs. This result confirms that speleothem magnetism is a valuable alternative tool for the study of paleosecular variation.

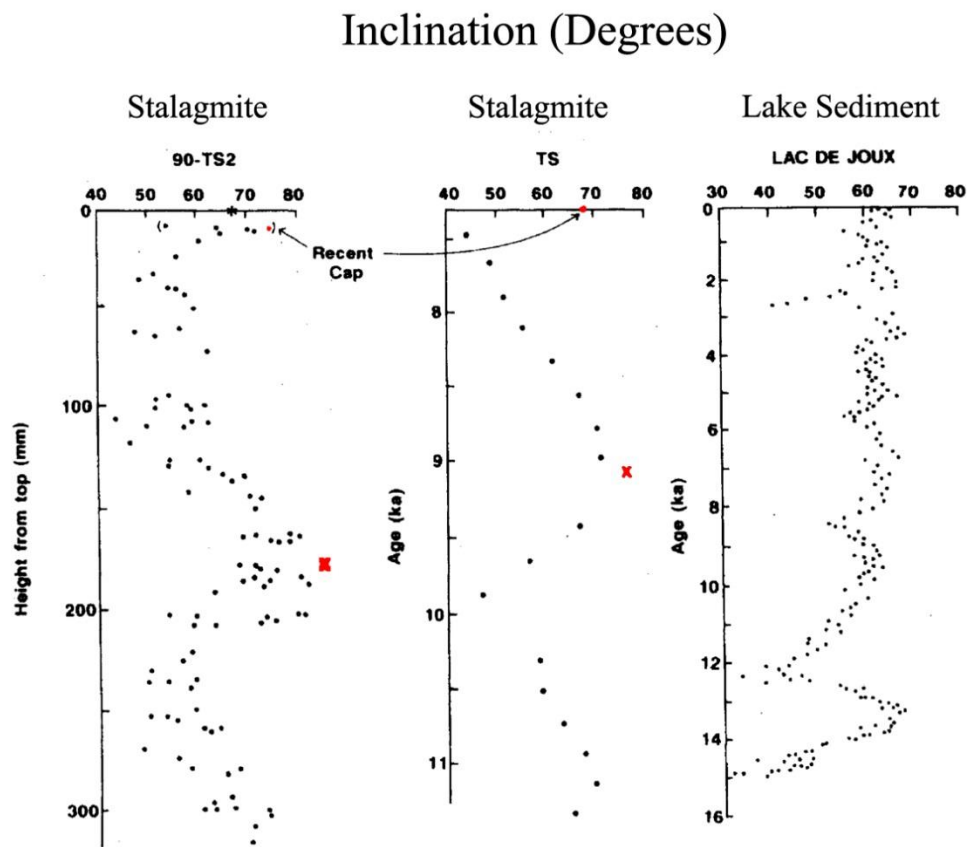


Figure 2.6: Inclination comparison between two stalagmites from the same cave and lake sediments, at the top, the red mark is referred to the recent direction and in middle a correlation point (Modified from Perkins & Maher, 1996).

Advances in multi-collector inductively coupled plasma mass spectrometry (Cheng et al., 2013) and in triaxial superconducting rock magnetometry in the late 1990's (Lascu & Feinberg, 2011) created the foundation for future research in speleothem magnetism. Lascu

& Feinberg (2011) summarized the major progress made in the Rock Magnetism community, not only with major advances in instrumentation but with the unmixing techniques and low-temperature SQUID magnetometry that enabled the recognition of different magnetic carriers in weakly magnetic rocks. After this review, several studies of speleothem magnetism started to appear in literature, including investigations of geomagnetic excursions (e.g., Osete et al. 2012; Lascu et al. 2016), magnetic mineralogy with focus on the origin and remanence in stalagmites (e.g., Zhu et al. 2012; Strauss et al., 2014; Strehlau et al. 2014; Font et al. 2014)) and studies of stalagmite magnetism as proxies for regional climate variability (Bourne et al., 2015; Xie et al., 2013).

At least two geomagnetic excursions were identified through the stalagmite record. The Blake excursion that around 114 kyrs, and characterized by anomalous inclination, was identified by Osete et al., (2012) in stalagmites from Spain. The Laschamp excursion occurred around 40 kyrs and is associated with the time of demise of *Homo neanderthalensis* in conjunction with rapid climatic oscillations leading into the Last Glacial Maximum. Lascu et al. (2016) were able to improve the age of the excursion by 2-3 times (Figure 2.7) with a combination of high-precision ^{230}Th dates and annual layer counting in stalagmites from different sectors of North America, proving the synchronicity of the Laschamp excursion regionally.

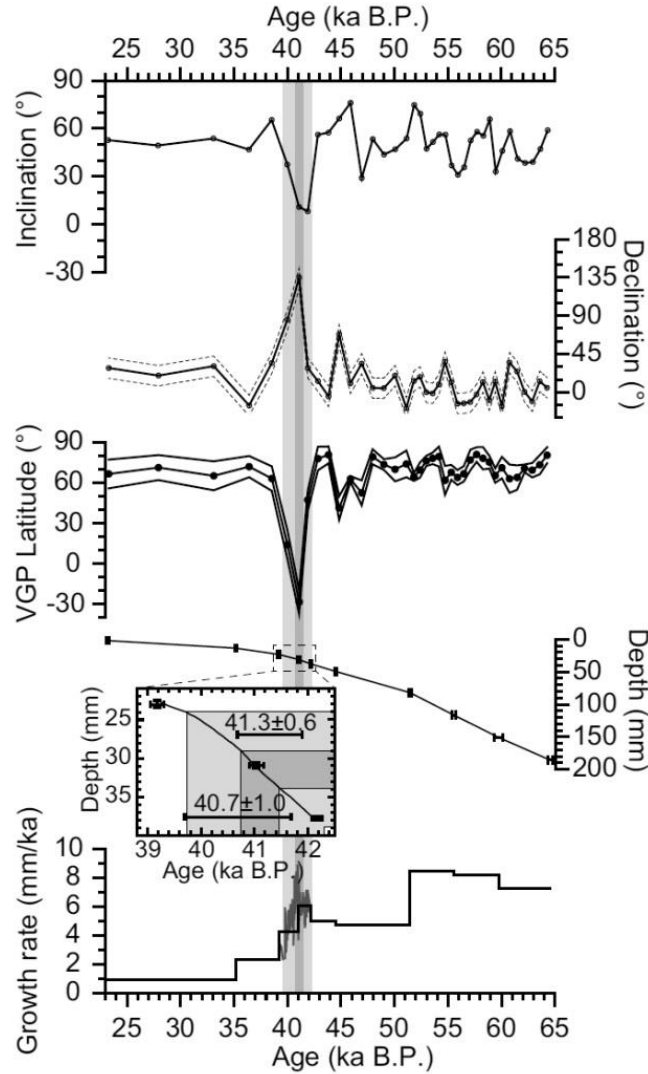


Figure 2.7: Age of Laschamp excursion determined by stalagmite records with magnetic properties (inclination, declination, VGP Latitude), age-depth model, incremental chronology and growth rates (Modified from Lascu et al., 2016).

The origin of magnetic remanence and its relation to hydrologic and climatic variation is the topic of the majority of studies after 2010 (Bourne et al., 2015; Font et al., 2014; Strauss et al., 2013; Strehlau et al., 2014; Zhu et al., 2012). Determination of grain size, shapes and elemental chemistry of magnetic carriers in stalagmites were reported by Strauss et al. (2013). In all samples, magnetite and goethite were found in varying abundances and morphologies. Magnetite grains displayed features characteristic of transport (evidence for detrital grains), including titanomagnetite grains and exsolved iron-titanium oxides identified through microscope analysis. Goethite grains were found in three different

morphologies – needle aggregates, solitary needles and polycrystalline aggregates. The main conclusion was that only magnetite and titanomagnetite can hold depositional remanence, and that goethite may be precipitated *in situ* on the stalagmite's drip surface. More recently, Bourne et al. (2015) identified a connection between large-scale climatic changes (precipitation) and the more localized processes of magnetic mineral cycling in soils overlying the cave systems. These authors found that changes in magnetite concentration follow changes in stable isotopes and other global climate proxies. The magnetic concentration time series was interpreted as a variation in local pedogenic processes, controlled by regional precipitation. The main magnetic assemblage in the studied caves is magnetite, produced by pedogenic processes, then transferred via dripwaters into the underlying cave-systems and incorporated into stalagmite. A similar conclusion was achieved by Zhu et al. (2012) using the remanence record of a Chinese stalagmite.

2.5 Soil magnetism

Natural rocks and soils comprise a complex assemblage of magnetic minerals with different compositions and grain sizes that result from iron oxide formation, dissolution or transformation. Almost all rocks contain some iron. During weathering, iron is released from rock-forming minerals and “secondary” pedogenic iron minerals are formed (Cornell & Schwertmann, 2003). The assemblages of magnetic minerals formed in well-drained soils are iron oxides, most frequently magnetite, maghemite, hematite, and goethite (Maxbauer, Feinberg, & Fox, 2016). The pedosphere is an environment of active mineral formation and transformation and exhibits a large variation in formation parameters in space and time over a range of scales. It openly and permanently communicates with neighboring compartments of the ecosystem (atmosphere, biosphere, hydrosphere, and lithosphere) so that equilibrium is usually not reached.

In oxic soils with $\text{pH} > 3$ the dissolution of ferrous iron-bearing primary minerals releases Fe^{2+} ions into the soil, and rapid oxidation occurs with the poorly soluble Fe^{3+} ions rapidly undergoing hydrolysis to precipitate ferrihydrite (Maxbauer, Feinberg, & Fox, 2016). When soil's pH is lower than 3, the formation of Fe^{3+} minerals must be mediated by micro-organisms (Cornell & Schwertmann, 2003). Ferrihydrite is unstable with respect to the more crystalline ferromagnetic and antiferromagnetic minerals and, with time, will progressively be converted into these more stable phases (Maxbauer, Feinberg, & Fox, 2016).

In the study of soils through rock magnetic techniques it is common to observe a magnetic enhancement between the upper A and B soil horizons. This arises primarily from the presence of superparamagnetic (SP) and stable single-domain (SSD) grains (Maher 2007; Liu et al. 2012, and references therein). There are two mechanisms to explain the ‘magnetic enhancement’ in well-drained soils:

- (1) Redox oscillations and the fermentation mechanism: the fermentation (anoxic condition) is the most significant pathway, where a redox oscillation during wet/dry cycles by reducing bacteria produces ultrafine magnetite, prone to oxidation towards

maghemite (Maher, 1997). Under anoxic conditions, the oxidation of organic matter is often coupled to the microbial reduction of Fe^{3+} -oxides in a process referred as Dissimilatory Iron Reduction (DIR). The DIR bacterium *Geobacter metallireducinis* (GS-15) was the first organism discovered that coupled degradation of organic matter (acetate) to the reduction of ferric iron leading to the extracellular precipitation of SP/SSD magnetite (Maxbauer, Feinberg, & Fox, 2016).

- (2) Aging pathways of ferrihydrite to hematite: the slow transformation of ferrihydrite into hematite, during which an intermediate ferromagnetic phase is produced is an alternative pathway that can lead to magnetic enhancement. The timescale for a full transformation of ferrihydrite into hematite is in the order of 10^5 - 10^6 years. Anoxic conditions are not necessary for this aging mechanism, therefore during a prolonged dry season the magnetic mineral production is primarily associated with ferrihydrite aging while in the rainy season the fermentation process is favored (Maxbauer, Feinberg, & Fox, 2016).

Transformation of ferrihydrite directly into goethite and hematite is common in soils and is dependent on the soil physicochemical conditions. Goethite is favored in cool, moist soils that only rarely experience prolonged aridity. By contrast, hematite is more abundant in subtropical, tropical soils with frequent episodes of prolonged dryness. Soils with near neutral pH and low organic content tend to favor hematite over goethite, and vice-versa (Maxbauer, Feinberg, & Fox, 2016). The presence of goethite and hematite in most of soils suggests that climate play an important role in the iron mineralogy of soils.

The major iron oxides in soils are magnetite, maghemite, hematite and goethite. Below there is a brief description of the magnetic properties of these minerals.

Magnetite (Fe_3O_4): the structure is cubic with inverse spinel; the O^{2-} ions form a slightly distorted cubic-close-packed lattice with Fe^{2+} and Fe^{3+} cations in interstitial sites. Fe^{3+} occupies all the tetrahedral A-sites while Fe^{2+} and Fe^{3+} occupy octahedral B-sites. The spin moments of A-site and B-site atoms are aligned antiparallel along the crystallographic 111 axis and are imbalanced because of Fe^{2+} ions within the B sub-lattice giving rise to magnetite's ferrimagnetism (Dunlop & Özdemir, 1997). The magnetic susceptibility (χ ; defined in Chapter 3) is usually $56500 \times 10^{-8} \text{ m}^3/\text{kg}$;

two important temperature transitions characterize pure magnetite grains: the Curie point at 580°C, where the thermal energy overcomes the exchange coupling and the ferrimagnetism is lost, and the Verwey transition at -150°C, a change in the crystallographic distribution of the iron ions, the previous cubic structure being slightly distorted into a monoclinic symmetry (Evans & Heller, 2003). Saturation magnetization (M_s ; defined in Chapter 3) is $\sim 92 \text{ Am}^2/\text{kg}$; coercivity (H_c) is low (tens of mT) and coercivity of remanence (H_{cr}) is usually 300mT (Maxbauer, Feinberg, & Fox, 2016).

Hematite ($\alpha\text{-Fe}_2\text{O}_3$): possesses hexagonal crystal structure in which alternate planes contain trivalent iron ions magnetized in opposite directions. The weak permanent magnetization is due to spin canting in neighboring planes that have magnetic moments nearly antiparallel within the basal crystallographic plane. The Curie point is about 675°C. On cooling the magnetization rises sharply to a plateau that is maintained down to the Morin transition at about -15°C, where the spin canting that causes weak ferromagnetism is lost. Susceptibility is usually $\sim 40 \times 10^{-8} \text{ m}^3/\text{kg}$. The saturation magnetization (M_s) is $\sim 0.4 \text{ Am}^2/\text{kg}$ and coercivity (H_c) is $\sim 150\text{-}350\text{mT}$ (Evans & Heller, 2003; Ozdemir & Dunlop, 2014; Maxbauer, Feinberg, and Fox 2016).

Maghemite ($\gamma\text{-Fe}_2\text{O}_3$): its chemical formula is the same of hematite, however they do not share the same crystallographic structure or magnetic properties. Maghemite is the oxidized form of magnetite (Fe_3O_4) and also presents a cubic symmetry. The Curie point is $\sim 645^\circ\text{C}$, but it is difficult to measure because the mineral is metastable. At elevated temperatures it suffers an irreversible crystallographic change to hematite with a loss of magnetization (Dunlop & Ozdemir, 1997). Susceptibility is lower than that of magnetite, usually $\sim 26000 \times 10^{-8} \text{ m}^3/\text{kg}$. The saturation magnetization (M_s) is $\sim 74 \text{ Am}^2/\text{kg}$; coercivity (H_c) is low (tens of mT) and coercivity of remanence (H_{cr}) is usually 300 mT (Maxbauer, Feinberg, & Fox, 2016).

Goethite ($\alpha\text{-FeOOH}$): it is orthorhombic and possesses a weak ferromagnetism originated from defects and substitutions within the crystal structure. Due to its

defect moment and the extremely weak saturation magnetization ($\sim 0.05\text{-}0.30$ Am²/kg), extreme high fields must be applied to deflect its moments. Susceptibility is usually $\sim 70 \times 10^{-8}$ m³/kg; the Néel temperature (which coincides with the Curie point) is about 120-150°C; it has a high coercivity (H_c) beyond 100 mT (Dunlop and Özden Özdemir., 1997; Maxbauer et al., 2016).

Chapter 3: Theoretical background of environmental magnetism

3.1 Rock magnetic measurements and environmental magnetic significance

Magnetic susceptibility is one of the most common properties used for rock magnetism and environmental magnetism studies. It relates the applied field (H) with the resulting induced magnetization (M). The volume susceptibility (κ) is expressed as the magnetization acquired per unit field:

$$\kappa = \frac{|M|}{|H|} \quad [3.1]$$

where κ is dimensionless in the *Système International* (SI) and M and H are expressed in A/m. Due to porosity variations that are commonly observed in speleothems (e.g. Strauss et al., 2013) and its irregular shape, mass normalized susceptibility (χ) is usually adopted. It is defined as the volume susceptibility divided by the density (ρ) of the material:

$$\chi = \frac{\kappa}{\rho} \quad [3.2]$$

where χ is expressed in m³/kg.

The field dependence of the induced magnetization is usually represented by a hysteresis loop (Figure 3.1). Starting with H = 0 and M = 0, the magnetization increases slowly with an applied field. On a stronger field, important changes in magnetic behavior occur. The magnetization reaches its maximum in a point called saturation of magnetization (M_s), where all moments are aligned with the applied field and it is not possible to increase the magnetization. Upon the removal of the field, the magnetization does not decrease to zero and attain instead a positive value, the remanence of saturation (M_r). To remove the magnetic remanence of a sample, an opposite field is applied until the magnetization reaches zero value; this is the coercivity force (H_c) (Figure 3.1). As the field continues to

be applied on the opposite direction, the point necessary to remove the remanence of saturation is called coercivity of remanence (H_{cr}). The hysteresis parameters can provide information about magnetic mineralogy composition and grain size.

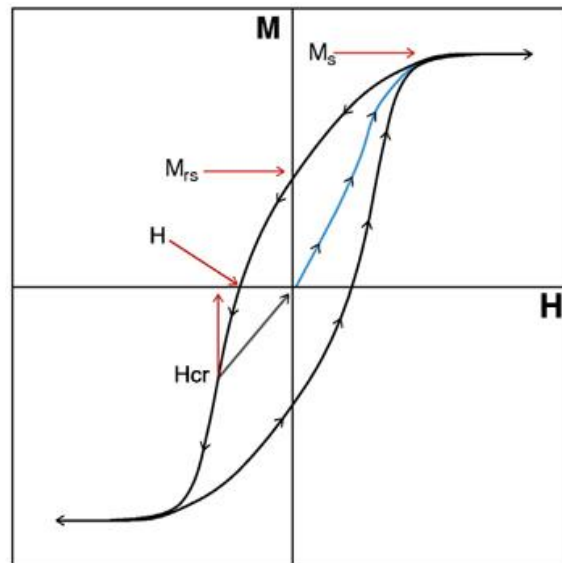


Figure 3.1: Examples of hysteresis loop; M_s =Saturation Magnetization; M_{rs} =Remanent saturation magnetization; H_c =Coercivity; H_{cr} =Remanent coercivity (Modified from Butler et al., 1992).

Magnetic domains are the elements of the microstructure of magnetic materials that link the basic magnetic properties of a material with its macroscopic properties (crystals); this magnetic property is a consequence of discontinuities in the equilibrium magnetization curve and of the demagnetizing effect. For a few hundred of nanometer, magnetite crystals break into regions of uniform magnetization (magnetic domains) to reduce overall magnetic energy (Liu et al., 2012). Multidomain grains (MD) have domain walls and respond differently to an applied field than single domain grains (SD) that are uniformly magnetized and have no domain walls. Between SD and MD size, there is another type of magnetic domain structure called pseudo single-domains grains (PSD), where the internal magnetic arrangement is structured in vortex or magnetic moments that fan out in “flower-like” structures (Liu et al., 2012). There is a fourth magnetic behavior called superparamagnetic (SP), that corresponds to the smallest grains ($< \sim 15$ nm) and is dominated by thermal

fluctuations. This occurs because although the exchange coupling is not overcome in these tiny particles, both remanence and coercivity drop to zero on any reasonable timescales of observation. Samples with a mixture of different domain structures show hysteresis curves with peculiar shapes, such as “wasp-wasted” and pot-bellied” (Tauxe, Mullender, & Pick, 1996), but unmixing the different magnetic contributions in hysteresis loops is always a challenging task (e.g. Dunlop, 2002; Jackson, Worm, & Banerjee, 1990). A summary of the critical sizes of the main magnetic grains can be found in Table 1.

Table 1: Critical grain sizes for some magnetic minerals (Dunlop and Ozdemir, 1997).

| Mineral | Superparamagnetic (SP) size (μm) | Single Domain (SD) size (μm) | Multidomain (MD) size (μm) |
|-----------|--|--|--|
| Magnetite | 0.025-0.030 | 0.050-0.084 | 0.3-4 |
| Maghemite | 0.03 | 0.06 | 0.166 |
| Hematite | 0.05-0.75 | 1 | 50 |

First-order reversal curves (FORC) were first proposed in an attempt to remove the ambiguity in hysteresis measurements (Pike, Roberts, & Verosub, 1999; a. P. Roberts, Pike, & Verosub, 2000). This diagram is based on partial hysteresis cycles and represents the most efficient method for mapping distributions of coercivities and interaction fields that exist at the nanometer scale (Harrison & Feinberg, 2008). The sample is first saturated at H_{sat} . The field is then decreased to a reverse field H_r . Measurements of a series of evenly spaced applied fields (H), from H_{sat} to H_r allows the construction of a series of magnetization curves, the *first order reversal curves*. The magnetization at a field H with reverse field H_r is denoted as $M(H_r, H)$, and the field spacing is denoted δH . Magnetization data from consecutive measurement points of a series of FORCs are then used to determine the FORC distribution, which is defined as a mixed second derivative (Roberts, Heslop, Zhao, & Pike, 2014):

$$\rho(H_r, H) = -\frac{1}{2} \frac{\partial^2 M(H_r, H)}{\partial H_r \partial H} \quad [3.3]$$

where the expression is divided by two because the magnetization switch from $+M_s$ to $-M_s$ has a magnitude of $2M_s$. In Figure 3.2, there is an example of a FORC diagram with each derivative. A smoothing procedure is required in this process because the second derivative tends to amplify the noise.

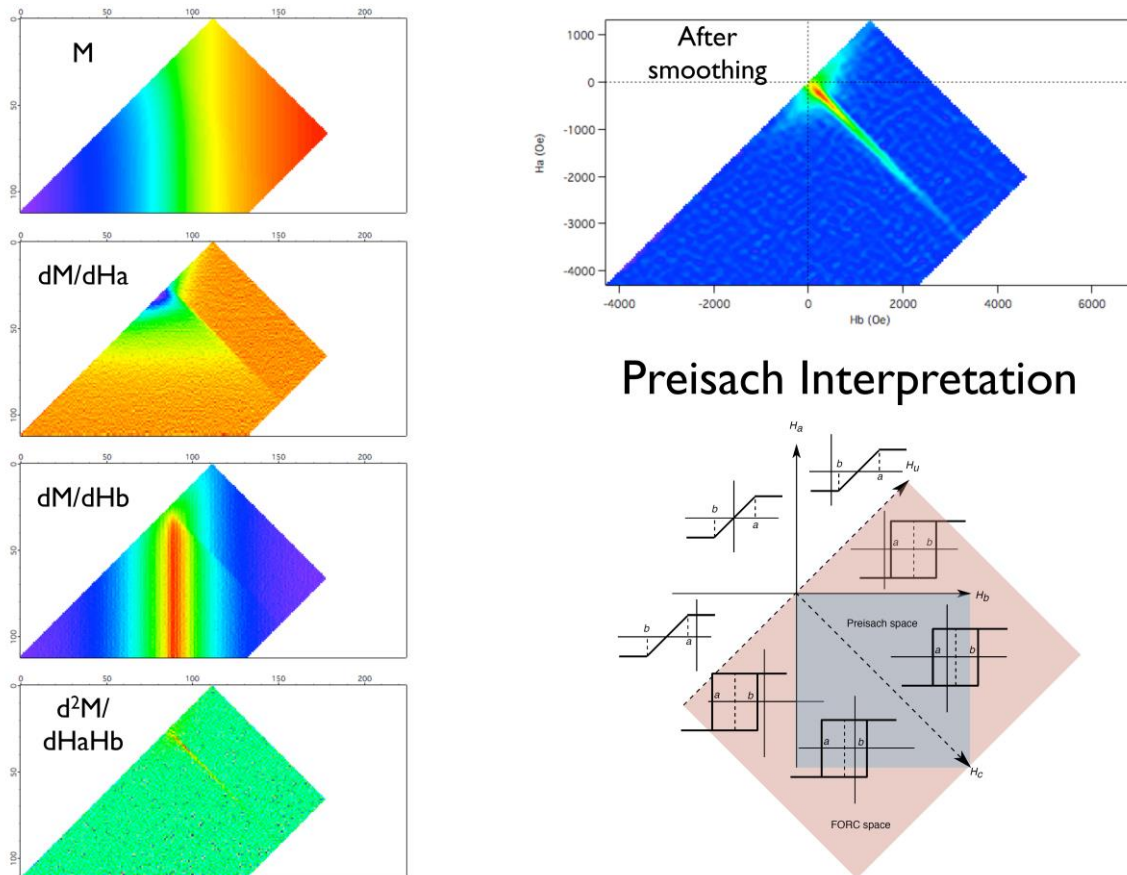


Figure 3.2: FORC diagrams, with each derivative (Harrison, 2015).

Interpretation of FORC diagrams is mainly qualitative, after the comparison of obtained results with an extensive database of natural and synthetic samples. Examples of typical FORC diagrams for single-domain, multi-domain, strongly interacting single-domain and pseudo-single domain grains are shown in Figure 3.3. Presently, numerical models are being developed to provide more robust and quantitative interpretations for FORC diagrams (Roberts et al., 2014).

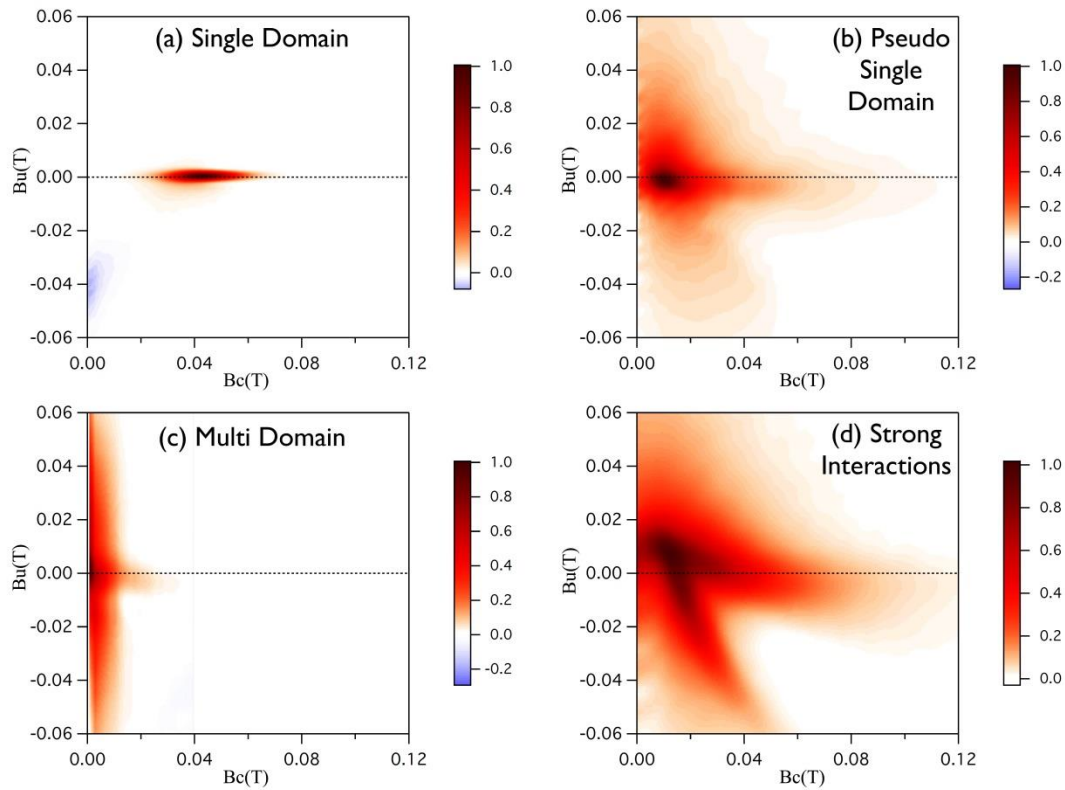


Figure 3.3: Domain state fingerprint from synthetic samples (Modified from Harrison, 2015).

Anhyseretic Remanence Magnetization (ARM) is an artificial remanence commonly used in environmental magnetism. It is obtained by subjecting the assembly of magnetic particles of a sample to an alternating and declining magnetic field (AF) superimposed to a small and constant direct field (DC). The sample will acquire an anhyseretic remanence magnetization (Collinson, 1983). ARM is a useful property for studies of SD particles containing ferrimagnetic materials because they acquire more remanence than the same volume of particles having domain walls because of their lower magnetostatic energy configuration. Based on this fact, (Cisowski, 1981) proposed a method to investigate the by comparing the ARM (or IRM) acquisition and ARM (or IRM) demagnetization curves. Non-interacting particles show symmetrical curves of magnetization acquired/demagnetized against the applied field. The crossover between both acquisition and demagnetization curves lies close to the remanent coercivity field in the magnetic field axis and also provides the ratio R along the normalized magnetization axis. R -values less than

0.5 indicate interactions between magnetic grains. Another parameter obtained from demagnetization/acquisition curves is the median destructive field (MDF) which corresponds to the field necessary to demagnetize half of the total magnetization.

Chemical and physical processes which affect the magnetic properties of a mixture of magnetic minerals in a sediment can often be associated to the climatic conditions during sedimentation (Egli, 2004). Magnetic unmixing techniques aim to identify these magnetic mineral components on the basis of their rock magnetic properties. Robertson and France (1994) proposed that acquisition/demagnetization curves of remanence magnetization with appropriate model functions could be used to separate the different magnetic components. According to these authors at first order each magnetic contribution in a given sample can be modeled as an independent cumulative log-Gaussian function (CLG). The parameters of the CLG (saturation remanence, remanent coercivity and deviation, DP) define the shape of each function. Therefore, a linear combination of model functions is expected to reproduce the acquisition/demagnetization curves. The individual cumulative log-Gaussian functions adjusted (Figure 3.4) provide information about coercivity distributions and total ARM (or IRM) of the different magnetic mineral components, and can be used to infer mineral type, grain size distribution and concentration of mixture components (Heslop, 2015).

Isothermal Remanence Magnetization (IRM) is acquired by exposing a sample to a strong steady field (pulsed field or DC field) at ambient temperature. By subjecting the sample to increasing applied fields the magnetization achieves its saturation, or the saturation remanent magnetization (SIRM). Larger fields ($>1\text{T}$) will tend to saturate antiferromagnetic materials (hematite, goethite), whereas smaller fields ($\leq 0.3\text{T}$) will saturate ferrimagnetic minerals (magnetite, titanomagnetite). Magnetic mineral unmixing can be performed in an IRM acquisition curve using an approach similar to that described above for ARM curves (Figure 3.4). Because the SIRM is independent of magnetic grain size, this technique provides a good parameter that reflects bulk magnetic mineral concentration (Liu et al., 2012). To separate the signal of the “hard” coercivity minerals (e.g., hematite, goethite) from the “soft” coercivity minerals (e.g., magnetite, maghemite), we can use IRM acquired with contrasting inducing fields. This separation makes possible to obtain two parameters, the HIRM (Hard-IRM) and the soft-IRM, expressed as:

$$\text{HIRM} = \frac{1}{2} (\text{SIRM} - \text{IRM}_{@0.3T}) \quad [3.4]$$

$$\text{Soft}_{\text{IRM}} = \text{SIRM} - \text{HIRM} \quad [3.5]$$

where HIRM is divided by two due to the contribution of the hard coercivity minerals in both SIRM and $\text{IRM}_{@300\text{mT}}$. Both parameters can be divided by the mass to reflect concentration of these magnetic minerals phases.

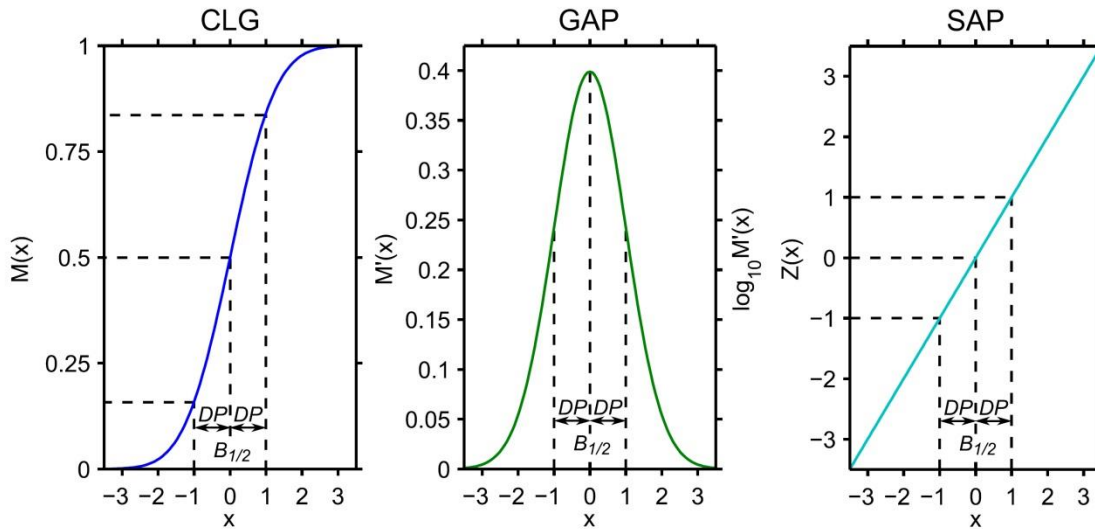


Figure 3.4: Cumulative log-Gauss (CLG) function proposed by Robertson and France (1994), the individual component is adjusted with median acquisition/demagnetization field ($B_{1/2}$); dispersion parameter (DP); saturation remanence magnetization (M). The gradient acquisition plot (GAP) obtained through the derivative of CLG. Standardised acquisition plot (SAP), ARM (or IRM) acquisition curve on a probability scale (modified from Heslop, 2015)

Another parameter that is widely used in environmental magnetic study is the S-ratio. This parameter reflects the change in the type of magnetic mineral. The S-ratio is given by:

$$\text{Sratio} = \frac{\text{IRM}_{@0.3T}}{\text{SIRM}} \quad [3.6]$$

The S-ratio is usually presented as percentage (%), representing the percentage contribution of the soft component.

The magnetic response of different magnetite and maghemite samples using the median destructive field (MDF) and the dispersion parameter (DP) after CLG function adjustment was obtained by (Egli, 2004). This study comprises samples from wind-blown dust, soils, loess, detrital grains, extracellular magnetite, aeolian dust, pedogenic magnetite and others. The MDF vs. DP diagram shows significant difference between the studied populations of grains and provide thus a “template” for the interpretation the origin of fine magnetite and maghemite particles.

The identification of magnetic populations with different coercivities can also be done using the approach proposed by Lowrie (1990), which consists in the three-axial IRM acquisition followed by stepwise thermal demagnetization of the sample. High (>1.2 T), medium (0.3 T) and low (0.1 T) magnetic fields are applied successively to the z, y and x axes of a sample and separate the contributions of hard (z-axis), medium (y-axis) and soft (x-axis) populations. Then, the unblocking temperatures revealed by the thermal demagnetization provide an independent parameter to identify the magnetic carriers.

Low-temperature saturation isothermal remanent magnetization (RTSIRM) measurements are used for the identification of small amounts of magnetic grains in a sample. These measurements are typically performed in a Magnetic Property Measurement System (MPMS) and allow one to identify the typical transitions of hematite (Morin transition at ~ 260K) and magnetite (Verwey transition at ~ 120K). Goethite is characterized by a factor of ~2 and an increase in remanence on cooling (Figure 3.5). In soils the Morin transition is suppressed due to defects and substitutions common to poorly crystalline hematite (Lascu & Feinberg, 2011).

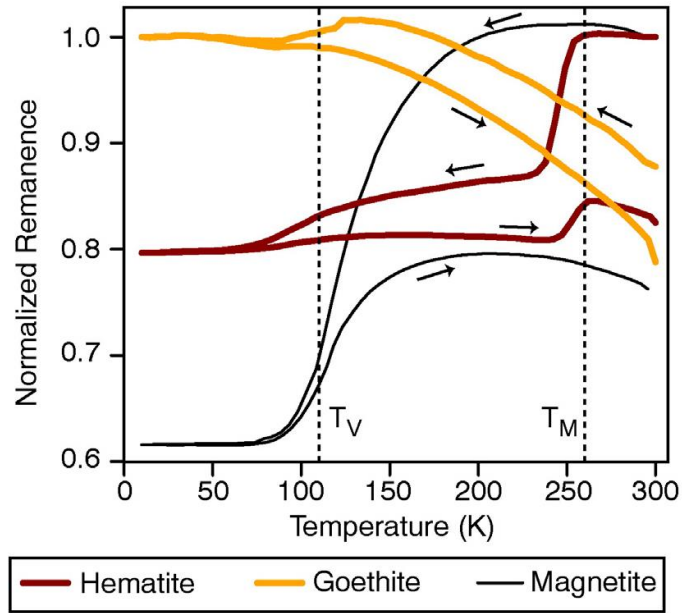


Figure 3.5: Example of Room-Temperature Saturation Isothermal Remanent Magnetization (RTSIRM) curves for hematite, goethite and magnetite; the arrows indicate remanence on cooling/warming, T_V = Verwey transition and T_M = Morin transition (extracted from Maxbauer et al., 2016).

Chapter 4: Methods

4.1 Sample preparation

The Alho 6 stalagmite sample is 240 mm long (z-axis) and 60 to 80 mm in diameter (top to bottom) (Figure 4.1). For magnetic measurements, the stalagmite was sliced with a diamond wire-saw into two halves. One half was subsampled for arbitrarily oriented specimens with 7 mm height (Z-axis, corresponding to the growth axis of the stalagmite), 20 mm length (X-axis) and 15 mm width (Y-axis), resulting in 34 discrete specimens (Figure 4.1).

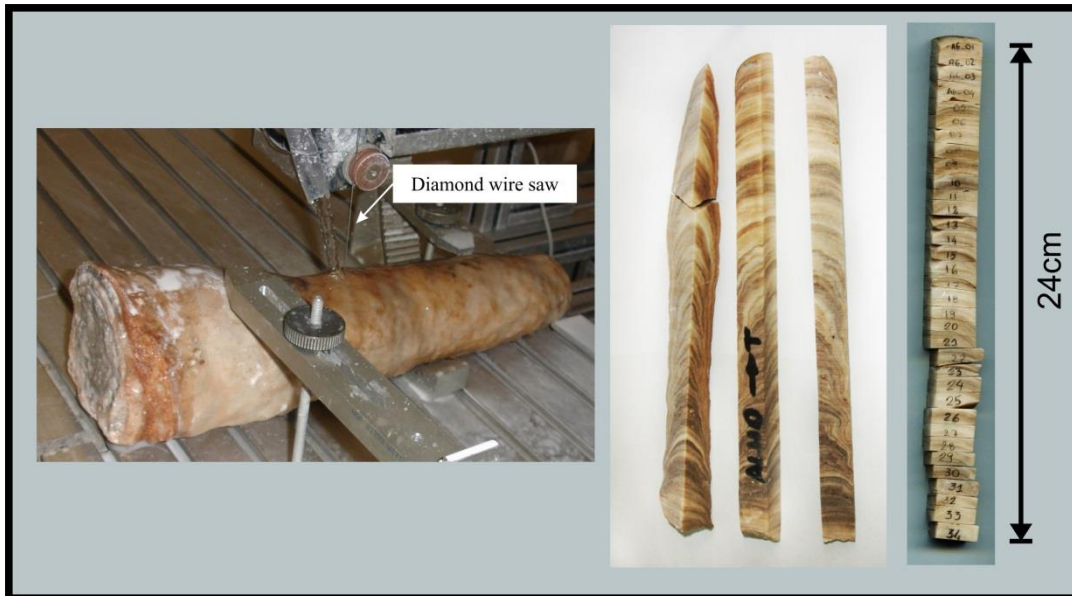


Figure 4.1: Sample Alho 6 from the Pau D'Alho cave; *left*, diamond wire-saw used to separate the stalagmite in two halves; *middle*, three slabs obtained; *right*, 34 discrete specimens obtained using a common rock saw.

In one sample (2 cm height from 9-11cm from the top), the magnetic extraction protocol of Strehlau et al. (2014) was applied. The protocol consists of a neodymium magnet coupled to an orbital shaker. Acetate buffer solution was used as a 4:1 ratio of 2 M CH_3COOH and 1 M NaCH_3COO for dissolution. A flask extraction is made with the neodymium magnet resulting in two subsamples: the extract, that contains strongly magnetic minerals such as

magnetite and maghemite, and the remainder, that tends to provide the weakly magnetic minerals (e.g., hematite and goethite). Both subsamples were studied with low-temperature magnetic techniques (see below).

In addition to the samples collected from the stalagmite, sediments inside and outside the cave were sampled to better constrain the origin of magnetic minerals in the stalagmite. These samples were only analyzed for ARM acquisition curves (see below).

4.2 Remanence measurements

Remanence measurements were made in a shielded room with ambient field <500 nT at the Laboratório de Paleomagnetismo of Universidade de São Paulo (USPmag). Natural Remanent Magnetization (NRM), Anhysteretic Remanent Magnetization (ARM), Isothermal Remanent Magnetization (IRM) were measured in a Superconducting Rock Magnetometer (SRM), manufactured by 2GTM. The sensitivity of this equipment is 10^{-12} Am². The Superconducting QUantum Interference Device (SQUID) monitors the differential change in the electric current flowing through a pair of Helmholtz-geometry superconductor pickup rings that is proportional to the magnetic moment of a sample in the center of the sense region (Kirschvink et al., 2015). The shape of the sample is not important, as long as the material being measured is contained within the uniform sense region (Kirschvink, 1992). In older magnetometers (e.g. astatic, induction-spinning and fluxgate-ring sensors) the shape of the sample is important.

Stalagmites have low concentrations of magnetic minerals. In order to obtain the best quality data, a study of the different configurations of the 2GTM SRM was carried. In this equipment, the user is able to select over how many counts the magnetic moment will be averaged between 1 and 90. For counts equal to 1 the measurement takes ~58 seconds to be completed, whereas for counts equal to 90 the measurement is completed in ~308 seconds. Using a standard sample provided by 2GTM, we performed tests varying progressively the number of counts (MM in Figure 4.2a). We observed a clear gain of sensitivity until count number of 6. After count number higher than 10 there is no clear increase in sensitivity (Figure 4.2b). We therefore set our counting number at 6, which was the most time-effective configuration.

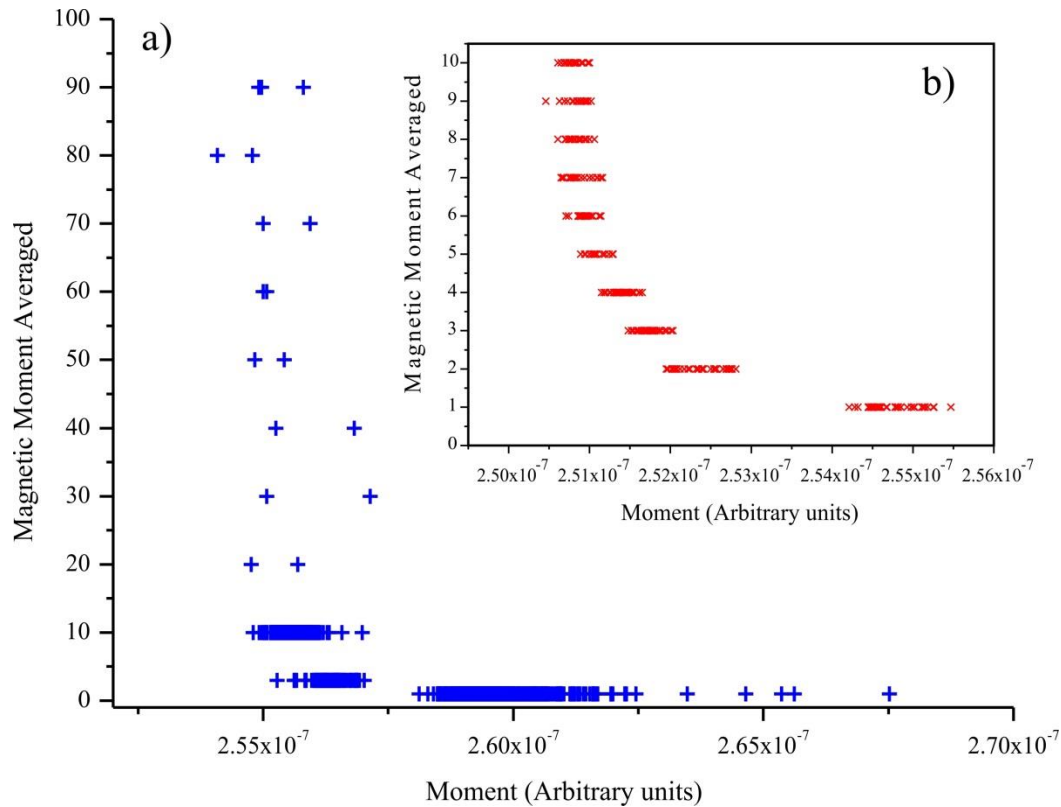


Figure 4.2: Testing the configuration of the superconducting rock magnetometer, (a) Large scale test, (b) Inset at fine scale.

Hysteresis loops and direct current demagnetization curves (DCD) were obtained in an Alternating Gradient Magnetometer (AGM) by Princeton Measurements Corporation MicromagTM 2900 also housed at the Laboratório de Paleomagnetismo of Universidade de São Paulo (USPmag). We carried the experiment in 23 samples (0.5x0.5 cm) varying the field from +1 to -1 T in 0.01 T steps. The FORC distribution included in this study was obtained after stacking the result of five independent measurements in order to improve the signal-to-noise ratio in these extremely weak magnetic rocks (Heslop & Roberts, 2012). The optimal choice of FORC parameters were the same as described in Egli et al., (2010) for smoothing a factor of five. FORC distributions were computed with FORCinel package (Harrison and Feinberg, 2008).

For the anhysteretic remanence magnetization (ARM) a direct bias field of 0.05 mT in Z-axis was adopted, with the alternating field varying from 1.5 to 200 mT in 32 steps. Using this procedure an acquisition curve of ARM and demagnetization curve (AF) were

generated enabling the Cisowski test. This procedure was performed with the u-channel SRM, where the user is able to write a script and run eight samples per time.

The isothermal remanence magnetization (IRM) acquisition curves were obtained at room temperature using the same u-channel SRM and the pulse magnetizer (MMPM10). The 34 specimens were subjected to pulsed fields along the Z-axis varying from 0.01 to 2.8 T in 37 steps, then three pulsed fields were imparted in the opposite direction (-Z-axis) at 0.01, 0.1 and 0.3 T to obtain the back-field values.

In addition to the Alho 6 samples, we also obtained ARM acquisition curves for sediments collected inside and outside de Pau d'Alho cave to allow a comparison between the magnetic mineralogy of the speleothem and that of eventual sources of magnetic carriers.

The Lowrie (1990) test was performed by thermally demagnetizing a three-axis IRM in 8 representative samples from the first quarter of the stalagmite (~15 mm height). Fields of 2.8 T, 0.4 T, and 0.12 T were successively induced along three perpendicular directions of the specimens using the MMPM10. Eighteen steps of thermal demagnetization were conducted up to 580 °C in a dual-chamber paleomagnetic oven manufactured by ASC Scientific. Magnetization measurements were performed using the u-channel SRM.

4.3 Low temperature experiments on bulk rock and magnetic extracts

Low-temperature experiments were performed on seven representative samples with a Magnetic Property Measurement System (MPMS) (Quantum Design) at the Institute for Rock Magnetism (IRM), University of Minnesota (UM). For six samples low-temperature experiments were made with bulk samples. In one sample the magnetic extraction protocol of Strehlau et al. (2014) described above.

Room-temperature saturation isothermal remanent magnetization (RTSIRM) curves were obtained in a field of 2.5 T at room-temperature, with the samples continuously measured in zero-field when cooled down to 10 K and warmed up to 300 K. For the FC-ZFC protocol, Field-Cooling (FC) curves were performed by applying a constant field of 2.5 T down to 10 K, whereas Zero-Field Cooling (ZFC) curves were performed in zero-field down to 10 K. In both cases, stepwise measurements were obtained at 5 K intervals.

Chapter 5: Results

5.1. Age of the Alho 6 stalagmite

The dating method and results used for the construction of the age-model of the Alho 6 stalagmite is described in Novello et al. (2016). These results were integrated in the present study since it corresponds to the same stalagmite studied here. In figure 5.01, we show the correspondence between samples, their age and the average time that each sample represents. The equation used is the one provided by Novello et al. (2016):

$$y = 1917.852 - 5.9362 \cdot x \quad [5.1]$$

where y is the age in years CE, and x is the distance from the top in mm.

| Sample # | Thickness (mm) | Age (CE) | Average years (CE) |
|----------|----------------|----------|--------------------|
| 1 | 9.0 | 1891 | 53.4 |
| 2 | 5.5 | 1882 | 32.6 |
| 3 | 6.7 | 1811 | 39.8 |
| 4 | 9.0 | 1764 | 53.4 |
| 5 | 6.6 | 1716 | 39.2 |
| 6 | 7.0 | 1680 | 41.6 |
| 7 | 5.6 | 1645 | 33.2 |
| 8 | 6.6 | 1603 | 39.2 |
| 9 | 7.3 | 1562 | 43.4 |
| 10 | 6.6 | 1508 | 39.2 |
| 11 | 4.9 | 1467 | 29.0 |
| 12 | 6.9 | 1431 | 41.0 |
| 13 | 6.5 | 1390 | 38.6 |
| 14 | 7.0 | 1372 | 41.6 |
| 15 | 6.8 | 1330 | 40.4 |
| 16 | 6.4 | 1289 | 38.0 |
| 17 | 6.4 | 1235 | 38.0 |
| 18 | 8.0 | 1188 | 47.4 |
| 19 | 6.0 | 1140 | 35.6 |
| 20 | 6.0 | 1105 | 35.6 |
| 21 | 6.5 | 1069 | 38.6 |
| 22 | 6.8 | 1016 | 40.4 |
| 23 | 5.4 | 974 | 32.0 |
| 24 | 7.0 | 938 | 41.6 |
| 25 | 7.2 | 888 | 42.8 |
| 26 | 7.1 | 837 | 42.2 |
| 27 | 6.0 | 802 | 35.6 |
| 28 | 6.5 | 760 | 38.6 |
| 29 | 6.0 | 725 | 35.6 |
| 30 | 5.8 | 683 | 34.4 |
| 31 | 7.0 | 648 | 41.6 |
| 32 | 5.3 | 600 | 31.4 |
| 33 | 7.3 | 576 | 43.4 |
| 34 | 7.6 | 535 | 45.2 |

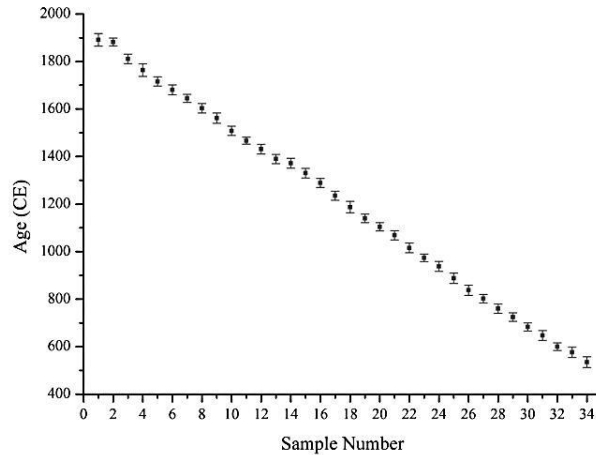


Figure 5.01: Sample number and the respective age, with the thickness of each sample and the average year that each sample comprehends. Ages (CE) by each sample number.

5.2 Oxygen and Carbon Isotope records

The oxygen and carbon isotope record has 1174 points. The oxygen isotope ratios have an average value of -6.17‰ , varying from -4.59 to -7.89‰ , and the carbon isotope ratios have an average value of -6.58‰ , varying from -3.84 to -8.72‰ . A moving average was calculated with 40 points for a better visualization of the data (Figure 5.02). Periods like MCA and LIA are evidenced by a distinct signature in the oxygen isotope record. MCA has constant and high values indicating a dry period, whereas LIA has near constant and low values indicating a humid period.

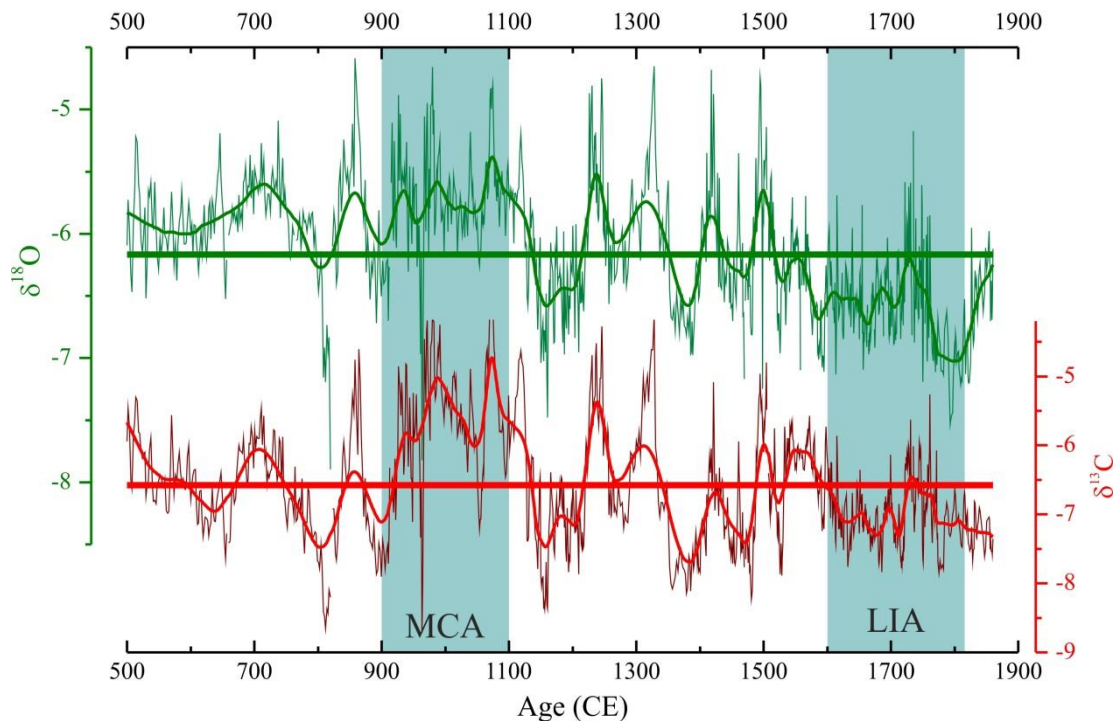


Figure 5.02: Isotope records from Alho 6 stalagmite, blue shades indicate the Medieval Climate Anomaly and Little Ice Age respectively.

Values of $\delta^{13}\text{C}$ and $\delta^{18}\text{O}$ data show moderate positive correlation ($r^2 = 0.46$). Besides the MCA and LIA events, the isotope record also shows intervals that depart from the average value. Positive peaks in $\delta^{18}\text{O}$ and $\delta^{13}\text{C}$ are observed at 709 CE and 858 CE, whereas negative peaks in $\delta^{18}\text{O}$ and $\delta^{13}\text{C}$ are observed at 812 CE and 893 CE. An interval of

dominantly positive $\delta^{13}\text{C}$ is observed between 1480-1600 CE that is not followed by a positive signal in $\delta^{18}\text{O}$.

5.2 Hysteresis and FORC diagrams

The 23 hysteresis curves from Alho 6 stalagmite show without exception a large contribution of the diamagnetic component due to the high amount of calcite. After slope correction (removal of the diamagnetic component) the low-coercivity magnetic phase is the dominant one. In figures 5.03 and 5.04, the hysteresis curves for eight representative samples before and after slope correction are shown.

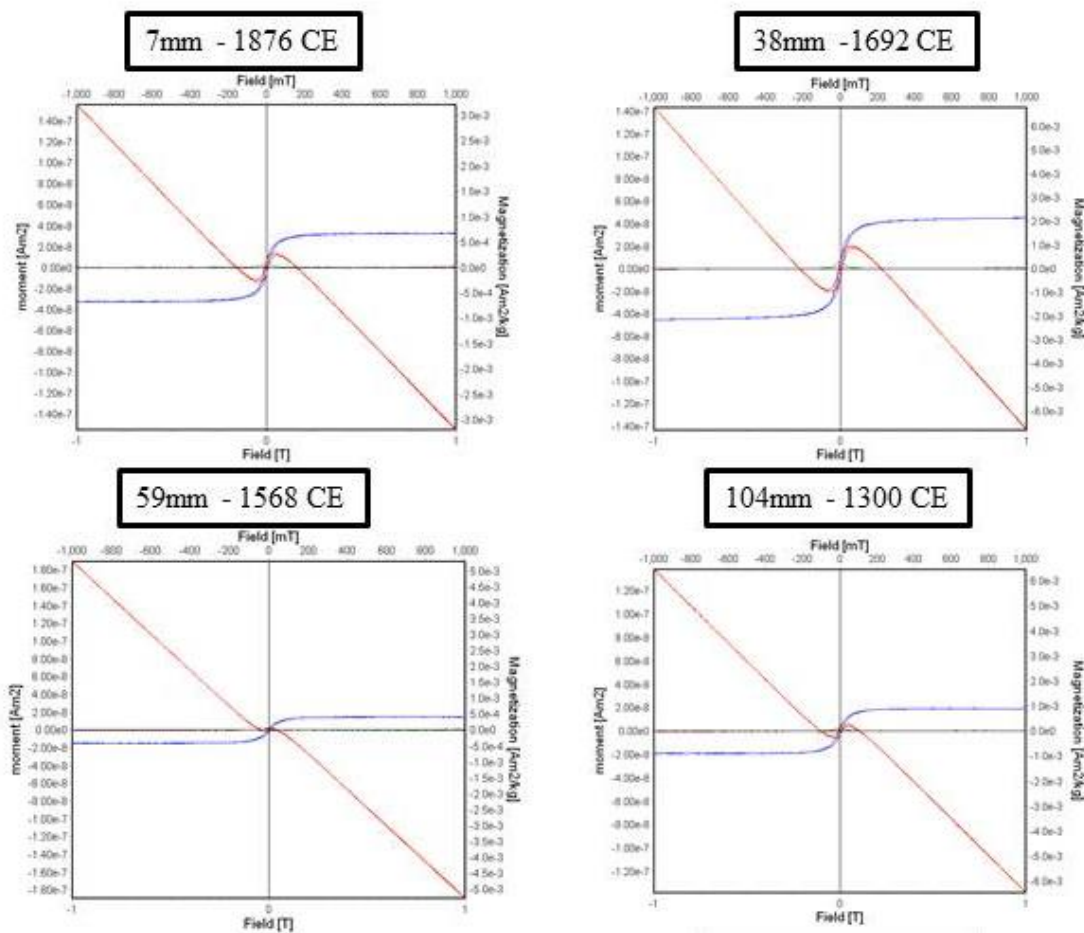


Figure 5.03: Hysteresis curves from four representative samples (1876 to 1300 CE) with their distance from the top (mm) and respective age (CE). Red lines represent the bulk measurement, and the blue line is the hysteresis curve after slope correction.

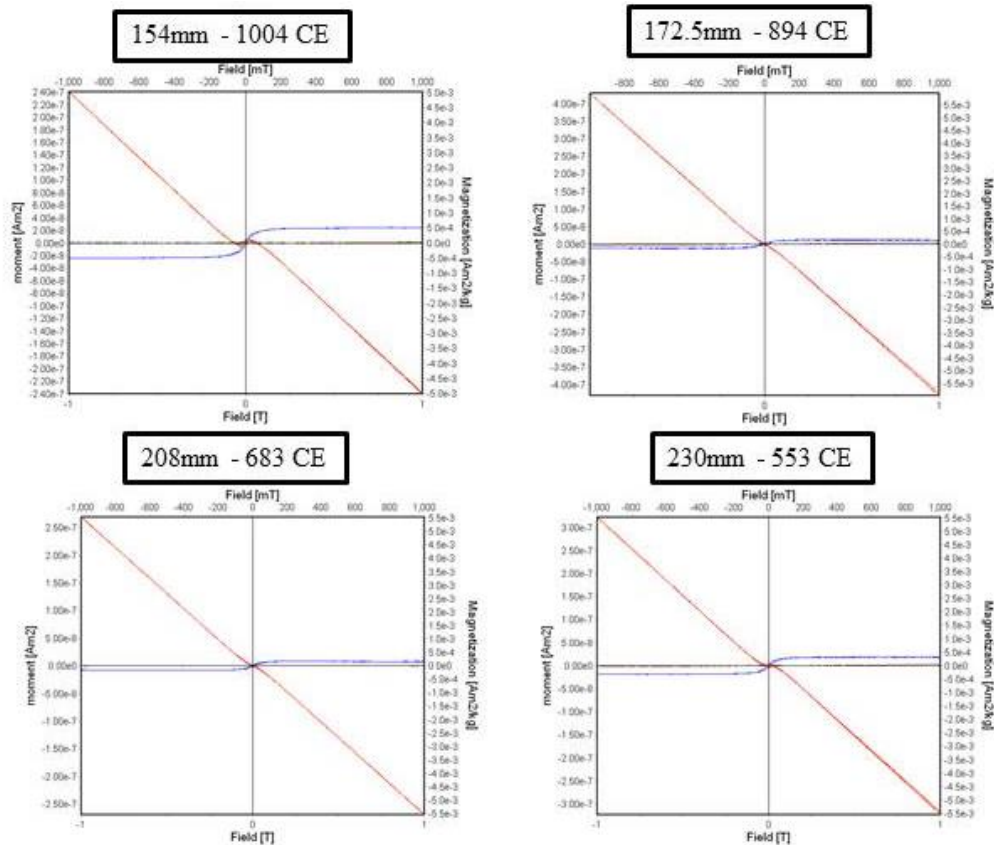


Figure 5.04: Hysteresis curves from four representative samples (1004 to 553 CE) with their distance from the top (mm) and respective age (CE). Red lines represent the bulk measurement, and the blue line is the hysteresis curve after slope correction.

FORC data were treated using the FORCInel software (Harrison & Feinberg, 2008). The smoothing factor selected was five, and the diagram was obtained after a stack of five independent measurements. Vertical and horizontal profiles were made to provide a better visualization of the diagrams (Figure 5.05). The FORC diagram and the profiles indicate a narrow central ridge, implying a low-coercivity mineral with single domain behavior.

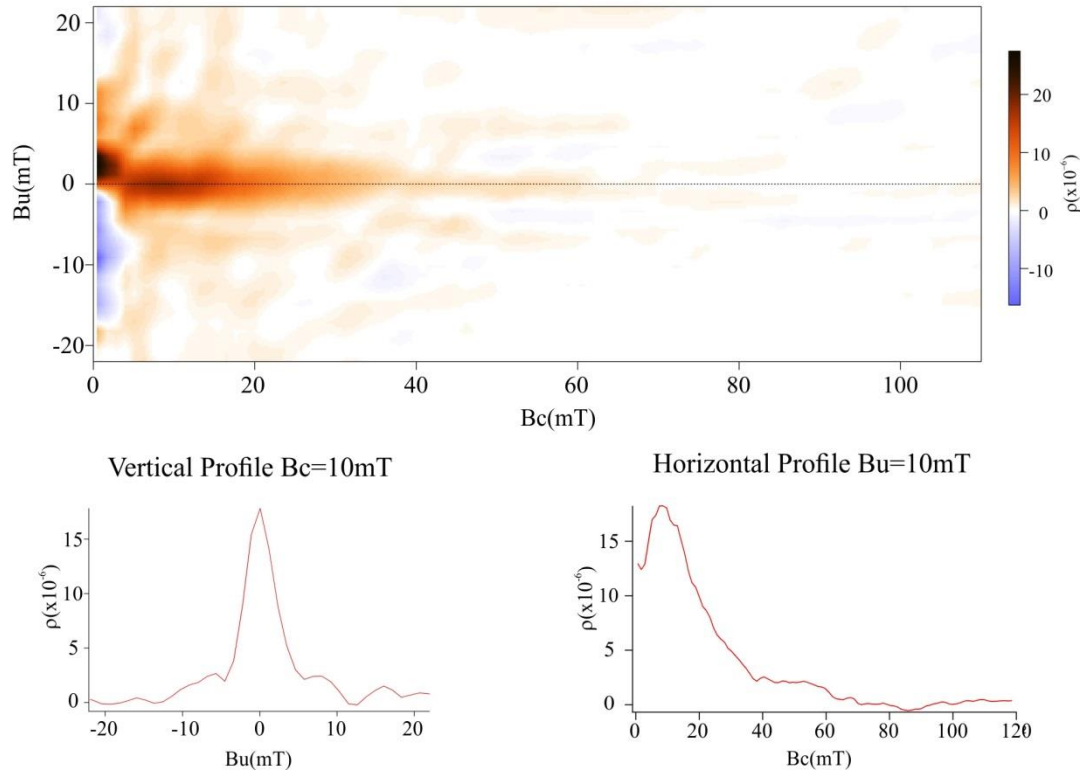


Figure 5.05: First Order Reversal Curves (FORC) diagram from Alho 6 stalagmite, exhibiting a narrow central ridge, with vertical and horizontal profile respectively.

5.3 ARM acquisition curves and Cisowski test

ARM acquisition curves for the 34 samples show the same behavior, indicating that the main magnetic carrier does not change throughout the stalagmite. In figure 5.06, four representative samples are shown and the results indicate a consistency with hysteresis and FORC analysis, where the low-coercivity fraction dominates de magnetic signal.

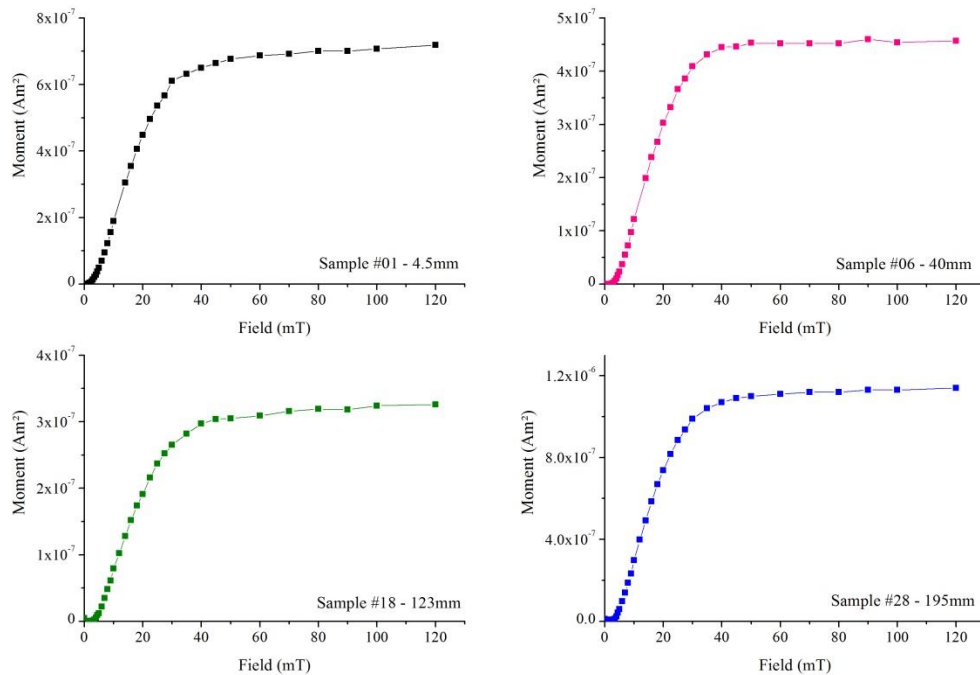


Figure 5.06: Anhysteretic Remanence Magnetization (ARM) acquisition curves of four different samples. The curves are very similar, indicating that the magnetic low-coercivity mineral is constant.

The acquisition of ARM in the sediments inside and outside the Pau d'Alho cave show the same behavior as the stalagmites ARM acquisition (Figure 5.07), indicating the presence of the same low-coercivity phase. The four samples for each component have the same signature, indicating the consistency of the magnetic signal.

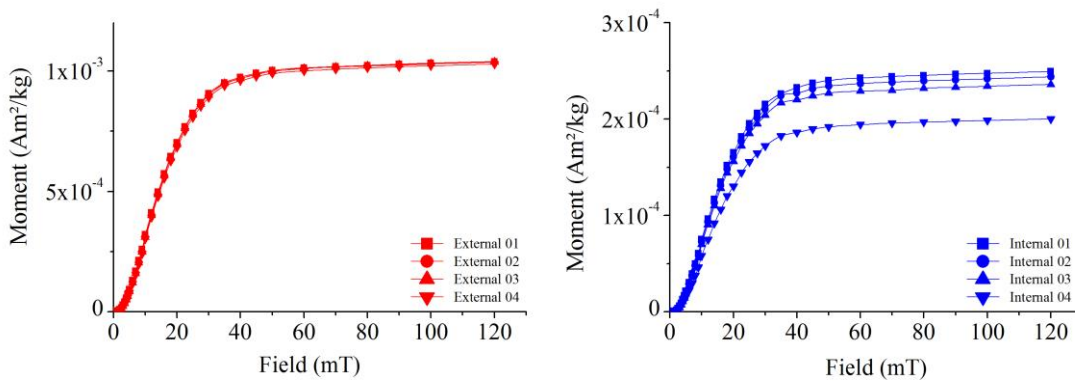


Figure 5.07: Anhyseretic Remanence Magnetization (ARM) acquisition curves of eight samples, the red line indicate the external sediments at the entrance of the cave and the blue line indicates the internal sediments in the cave. The curves are very similar, indicating that the magnetic low-coercivity mineral is constant.

Results obtained with the Cisowski test further emphasize the homogeneity of the magnetic mineralogy throughout the stalagmite (Figure 5.08), with R-values varying within a narrow range between 0.42 and 0.46 (average of 0.44) and H-values varying between 13 and 16 mT (average of 14 mT). R-values for non-interacting SD particles should be 0.5. Values lower than this show that there is some degree of interaction and this is in good agreement with FORC analysis. In figure 5.08, two representative samples are shown, with the histogram from H-values and R-values for the 34 samples.

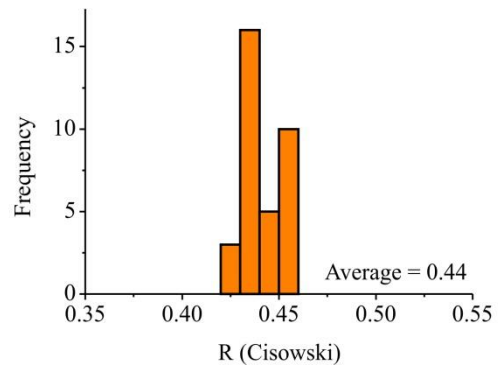
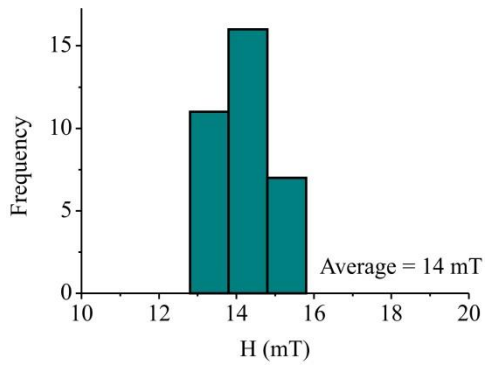
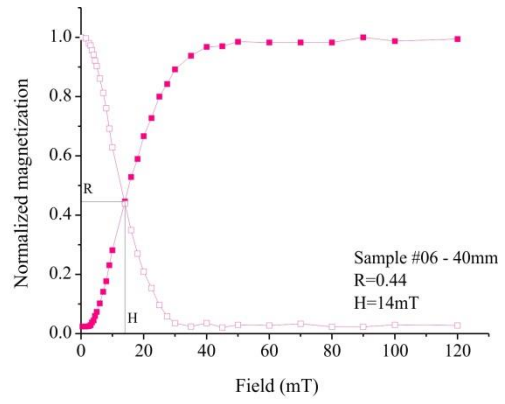
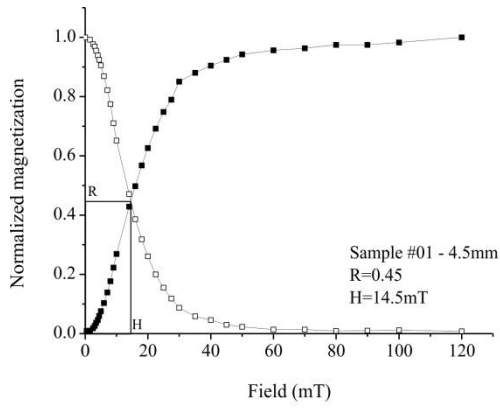


Figure 5.08: Examples of Cisowski test obtained for two samples and the histogram from H-values and R-values respectively.

5.4 IRM acquisition curves and Lowrie test

The isothermal remanence magnetization (IRM) curves also show a similar behavior throughout the stalagmite. Four representative samples are plotted in Figure 5.09. The low-coercivity magnetic phase (<300mT) contributes with more than 90% of the magnetization and a high-coercivity magnetic phase (>300mT) is clearly present because the magnetization does not reach the saturation with the highest field.

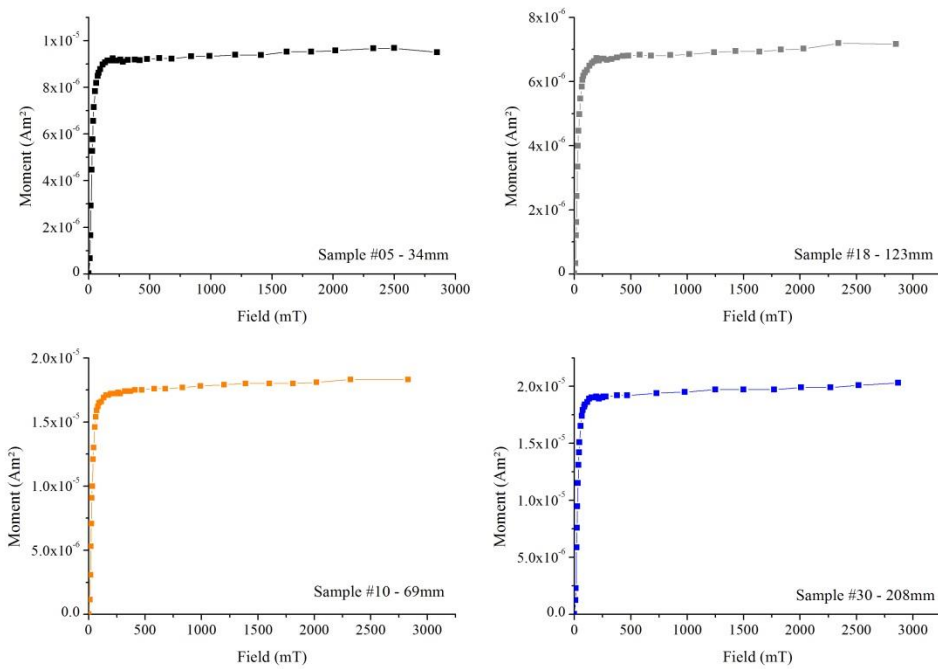


Figure 5.09: Isothermal remanence magnetization (IRM) curves obtained for Alho 6 stalagmite, four representative samples are plotted with evidence of low- and high-coercivity phase.

Thermal demagnetization of 3-axis IRMs typically show the dominance of a soft magnetic component, which demagnetizes at $\sim 560^{\circ}\text{C}$. The medium coercivity phase is almost negligible, but when present it unblocks at roughly the same temperature (Figure 5.10). The hard component is also small to negligible in most samples. In some samples there is a slight increase in magnetization at $\sim 120^{\circ}\text{C}$ that may be due to the presence of goethite (see low-temperature MPMS results below). It is worth noting the absence of

remanent carriers with unblocking temperatures higher than 600°C, suggesting that hematite is not a significant remanence carrier in these samples. Four representative samples are shown in Figure 5.10 with their respective applied fields.

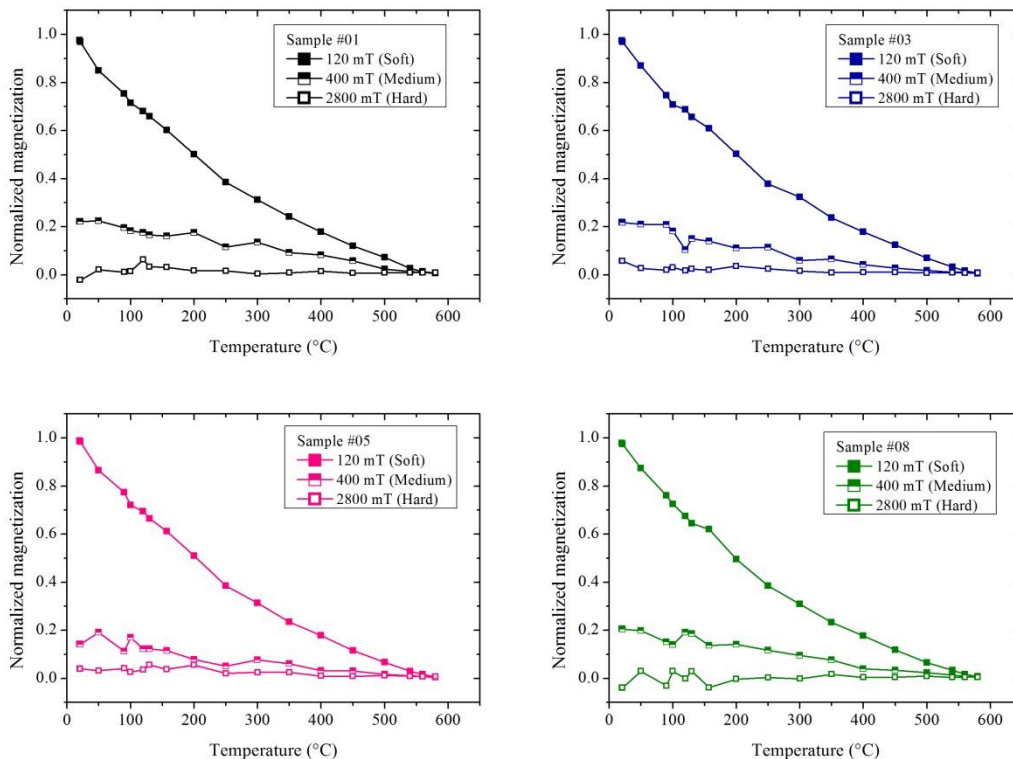


Figure 5.10: Thermal demagnetization of three-axis, four representative samples indicates the main contribution of the soft-coercivity phase with unblock temperature of ~560°C.

5.5 Unmixing methods and remanence ratios

The analysis of ARM curves for all 34 specimens shows a low-coercivity fraction with $B_{1/2}$ of 15.1-17.0 mT (average of 16 mT) and dispersion parameter (DP) between 0.27-0.31 (average of 0.29) (Figure 5.11). A cumulative log-Gaussian function (CLG) was calculated with Kruiver et al. (2001) workbook for all samples. An example of the gradient is plotted in Figure 5.11 with the respective histogram of the adjusted component.

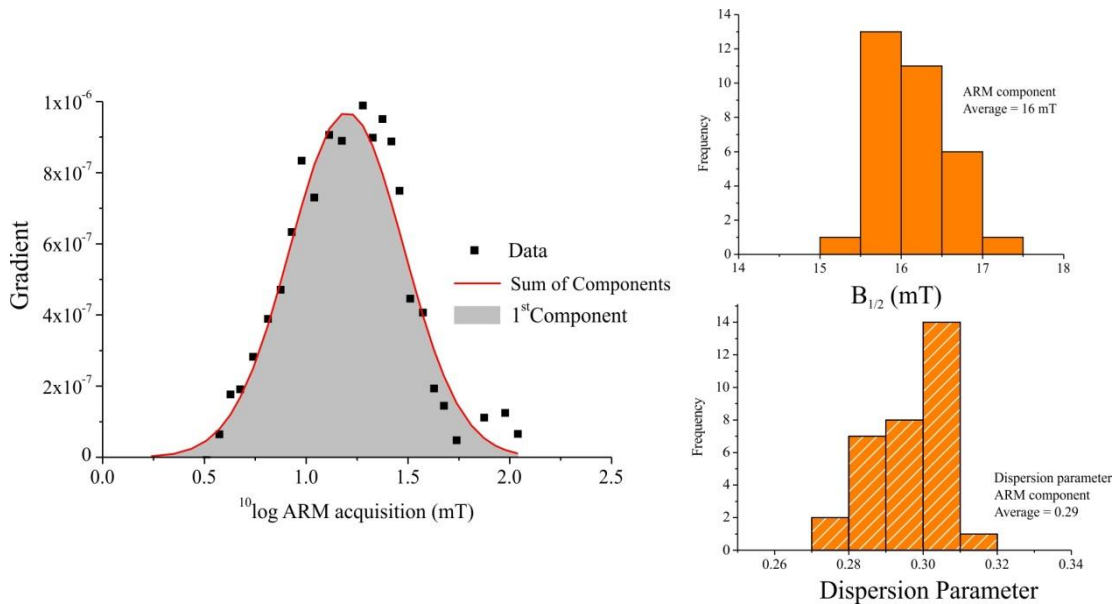


Figure 5.11: Example of cumulative log-Gaussian function adjusted for Alho 6 stalagmite, with a histogram of the $B_{1/2}$ and dispersion parameter of all samples.

Results from the unmixing of IRM acquisition curves are in good agreement with the parameters derived from ARM curves, with the $B_{1/2}$ values of 24-28 mT (average of 26.2 mT) and DP between 0.25-0.31 (average of 0.28), and a high-coercivity fraction with $B_{1/2}$ of 1260-3980 mT (average of 2557 mT) and DP between 0.8-1.0 (average of 0.9). The high-coercivity fraction was not accurately defined given its low content and the fact that the magnetization did not reach saturation with the maximum applied field of 2800 mT. In Figure 5.12, an example of a gradient of cumulative log-Gaussian function (CLG) used to adjust the IRM is plotted together with histograms of $B_{1/2}$ and DP.

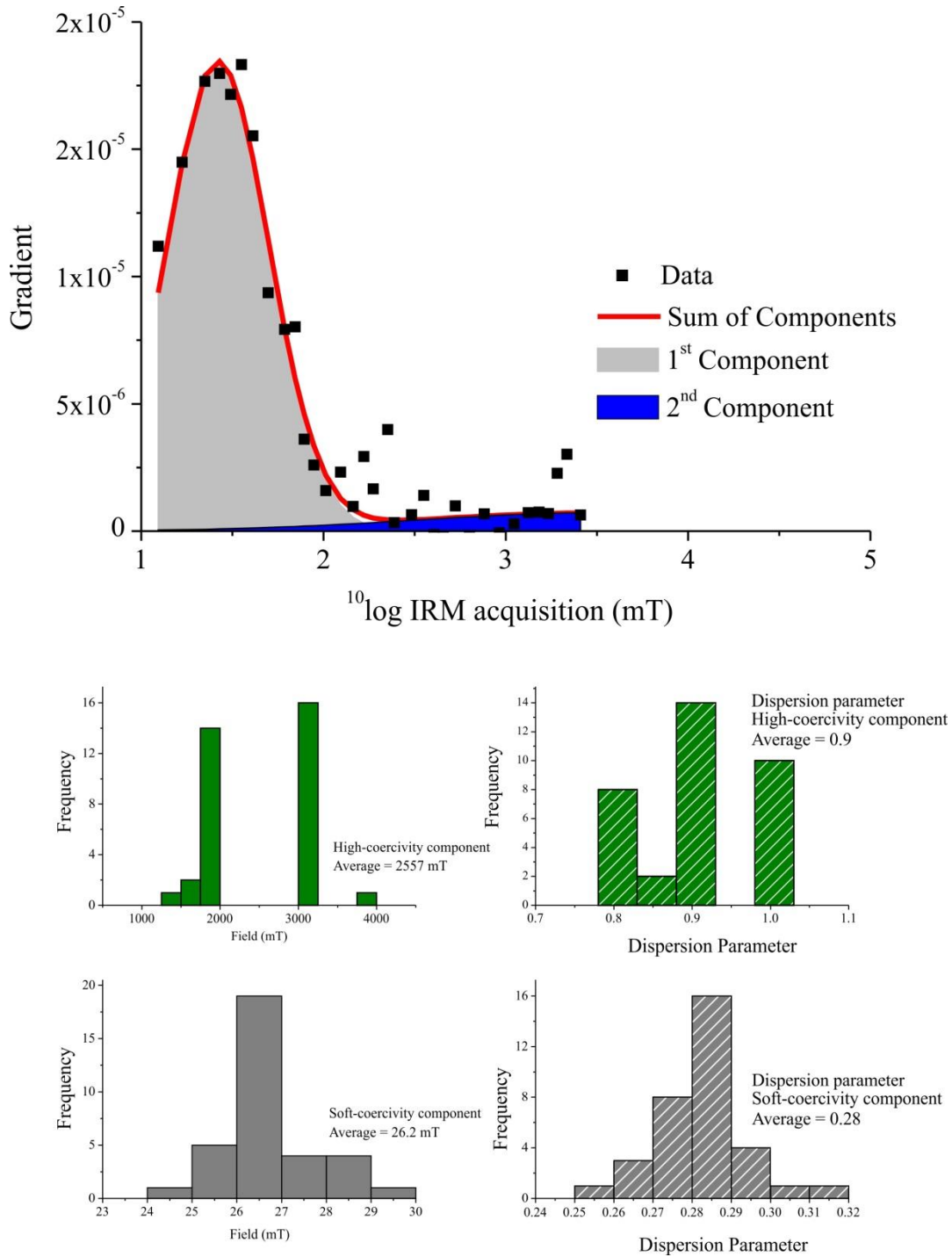


Figure 5.12: Example of a gradient of the cumulative log-Gaussian function adjusted for Alho 6 stalagmite, with a histogram of the $B_{1/2}$ and dispersion parameter of all samples.

The unmixing of ARM acquisition curves from sediments inside and outside the Pau d'Alho cave are in good agreement for all these samples, with the $B_{1/2}$ values of 14.8-15.1

mT (average of 15 mT) and DP between 0.30-0.32 (average of 0.31). These results are within the range observed in the stalagmite.

The intensities of remanent magnetizations (NRM, ARM and SIRM) throughout the Alho 6 stalagmite are broadly consistent (Figure 5.13) (see Appendix 1 for a table showing the values of remanence magnetizations). NRM varies from $\sim 1.1 \times 10^{-7}$ to $\sim 1.5 \times 10^{-6}$ Am²/kg, ARM varies from $\sim 4.5 \times 10^{-7}$ to 3.6×10^{-6} Am²/kg, SIRM varies from $\sim 1.2 \times 10^{-5}$ to $\sim 7.5 \times 10^{-5}$ Am²/kg, HIRM varies from $\sim 6.4 \times 10^{-7}$ to $\sim 3.5 \times 10^{-6}$ and soft-IRM varies from $\sim 1.1 \times 10^{-5}$ to 7×10^{-5} Am²/kg. All magnetic parameters covary throughout the stalagmite (Figure 5.14), including those that highlight the low-coercivity fraction (e.g., ARM, soft-IRM). A linear regression coefficient (r^2) was calculated for all the parameters that express variation in concentration. All r^2 values are positive and higher than 0.67, indicating that the magnetic minerals expressed by natural and artificial remanences and by the different remanence ratios can be explained by the same origin.

The S-ratio parameter varies from 0.87 to 0.92 (mean of 0.90) (Figure 5.13) and are similar to those found in other speleothems (e.g. Font et al., 2014). This result implies that 90% of the magnetization can be attributed to the low-coercivity fraction.

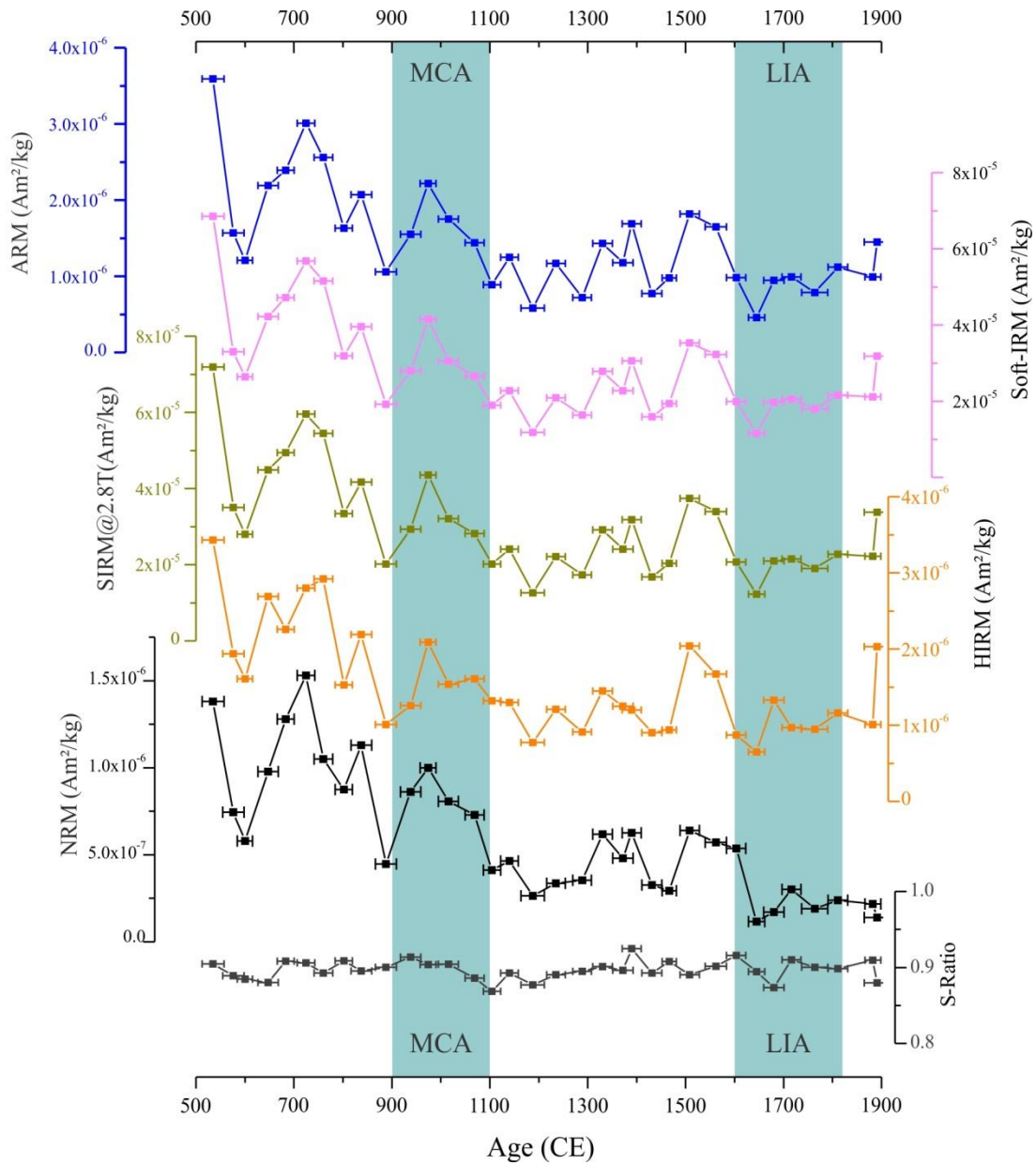
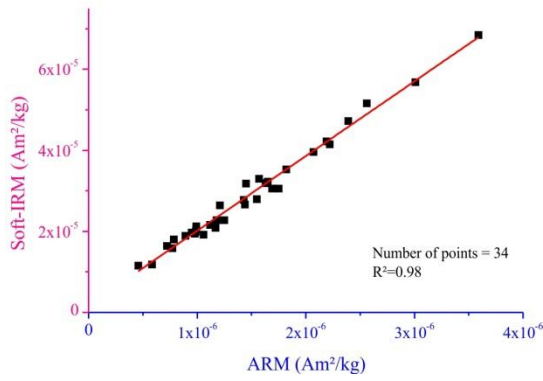
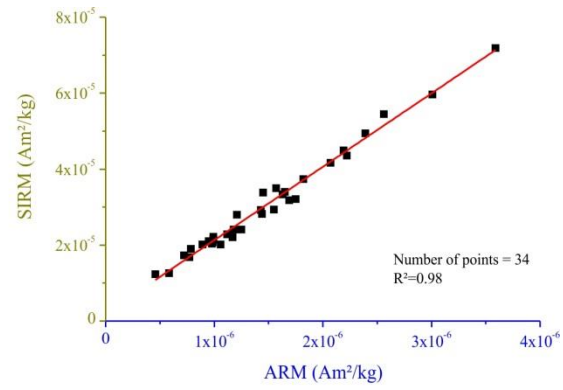
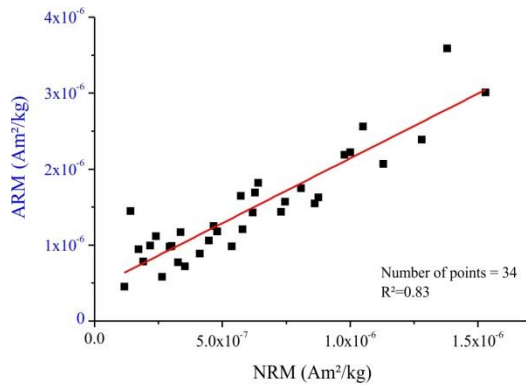


Figure 5.13: Magnetic remanence values: ARM (anhysteretic remanent magnetization), Soft IRM (soft component of IRM acquisition curves), SIRM (saturation remanent magnetization), HIRM (high-coercivity isothermal remanent magnetization), NRM (natural remanent magnetization) and S-ratio. Blue shades indicate the Medieval Climate Anomaly and Little Ice Age respectively.



| | NRM | ARM | SIRM | HIRM | Soft-IRM |
|----------|------|------|------|------|----------|
| NRM | 1.00 | | | | |
| ARM | 0.83 | 1.00 | | | |
| SIRM | 0.79 | 0.98 | 1.00 | | |
| HIRM | 0.67 | 0.88 | 0.93 | 1.00 | |
| Soft-IRM | 0.80 | 0.98 | 1.00 | 0.92 | 1.00 |

Figure 5.14: Linear regression (r^2) of the magnetic remanence data, and a table with the values of the r^2 of the different remanence magnetizations.

5.6 Low-temperature SQUID magnetometry (FC-ZFC, RTSIRM)

Six bulk samples distributed along the stalagmite produced similar MPMS low-temperature curves, which are typical of a mixture between magnetite and goethite (Figure 5.15). RTSIRM curves typically show the Verwey transition (Figure 5.15) characteristic of magnetite. In addition, these data also indicate the presence of goethite, identified by the separation between FC-ZFC curves between 10 and 300 K (high-coercivity component) (Guyodo et al., 2006; Maxbauer et al., 2016) and is similar to results obtained in other stalagmites (Lascu & Feinberg, 2011; Strauss et al., 2013). This interpretation is reinforced by the decreasing trend on warming observed in RTSIRM data (Strauss et al., 2013). The absence of Morin transitions in low-temperature curves suggests that hematite does not contribute significantly to the high-coercivity signal in Alho 6, although it should be noted that many forms of natural hematite show muted Morin transitions. These results allow us to identify the two phases that dominate the remanence throughout Alho 6 stalagmite as magnetite and goethite, which correspond respectively to the low- and high-coercivity phases observed in other measurements.

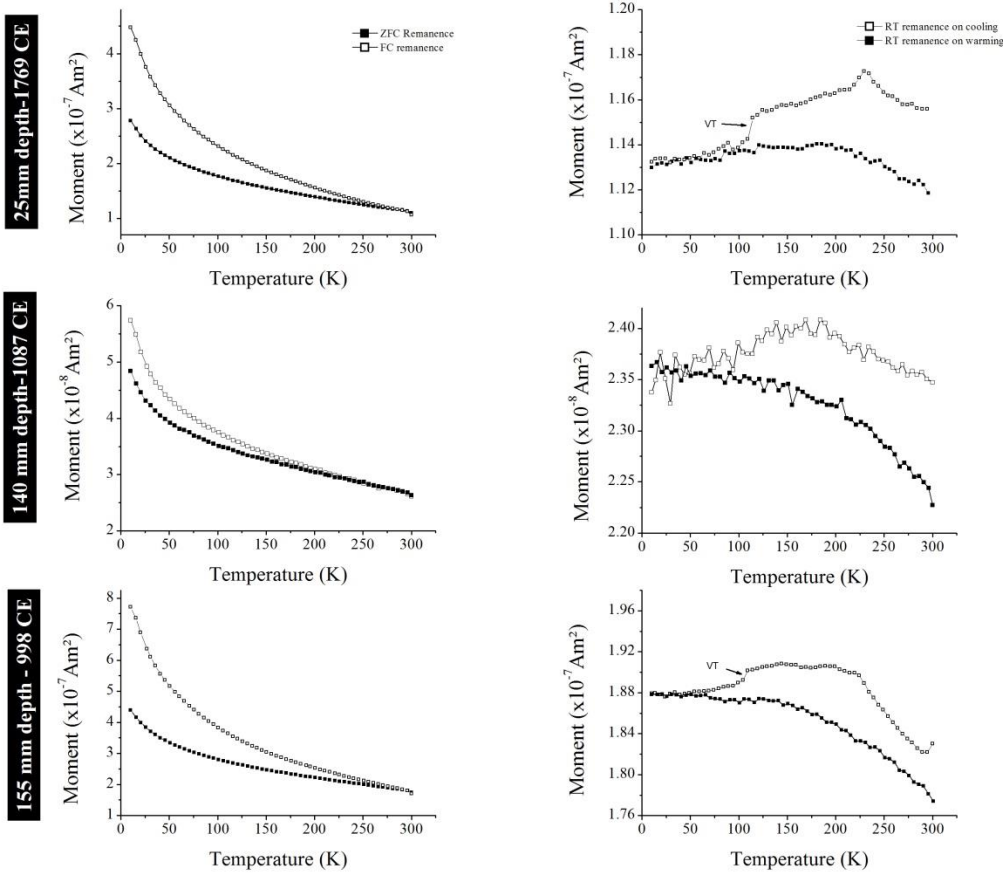


Figure 5.15: Low-temperature remanence measurements for samples collected at 25 mm depth; 140 mm and 155 mm depth from the top of the stalagmite. FC: Field Cooling; ZFC: Zero Field Cooling; RT: Room-temperature saturation isothermal remanent magnetization; VT: Verwey Transition.

Analyses performed in the magnetic extracts and in the remainder material confirmed the results obtained with the bulk samples. After extraction the Verwey transition was improved in the RTSIRM data for the extract (Figure 5.16), and the negative slope associated with goethite was emphasized in the remainder material after extraction (Figure 5.16). FC/ZFC curves show a similar behavior in both extract and remainder, with separation between FC-ZFC curves between 10 and 300 K.

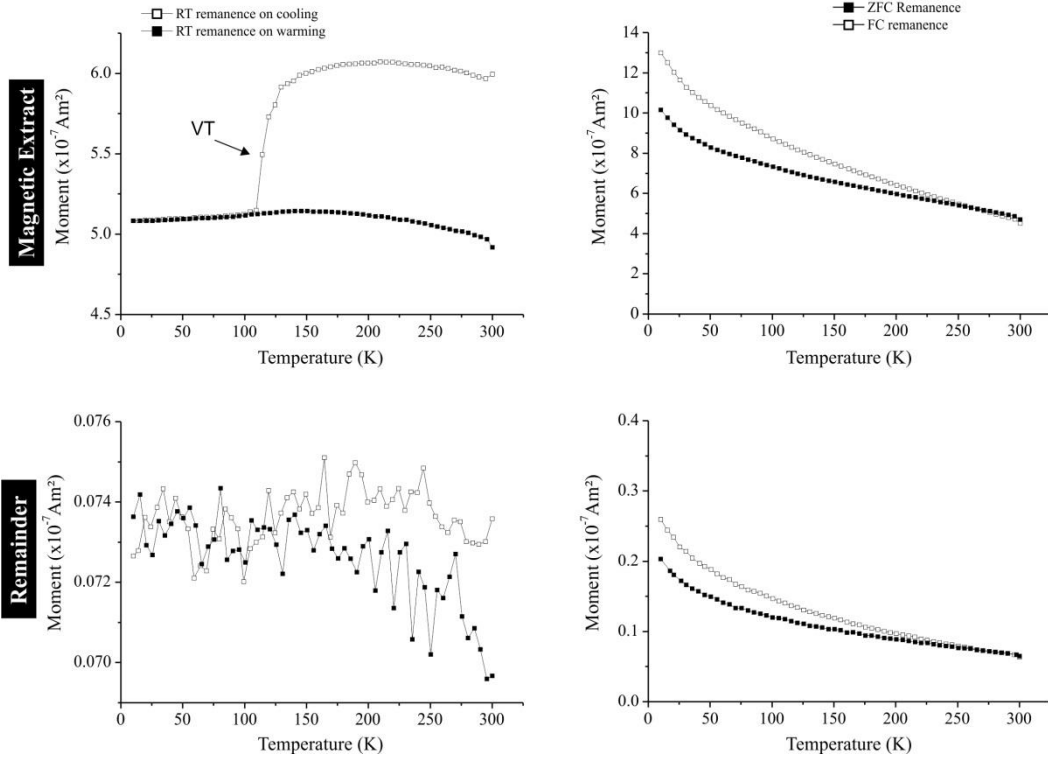


Figure 5.16: Low-temperature remanence measurements of the magnetic extract (low-coercivity mineral) and the remainder (high-coercivity mineral) for the sample Alho 6 stalagmite. FC: Field Cooling; ZFC: Zero Field Cooling; RT: Room-temperature saturation isothermal remanent magnetization; VT: Verwey Transition.

Chapter 6: Discussion

6.1 The source of magnetic minerals

Magnetic measurements indicate that the main magnetic remanence carriers in Alho 6 stalagmite are magnetite and goethite, occurring in a nearly constant relative proportion. The same phases have been identified in other stalagmites by Perkins et al. (1996), Lascu & Feinberg (2011), Strauss et al. (2013) and Strehlau et al. (2014). Magnetite grains have remanent coercivities varying between 14-17 mT (from ARM acquisition curves and FORC diagrams). To infer the origin of the low-coercivity phase, our data can be further compared with Egli's (2004) database for detrital, pedogenic and organically formed magnetite in which the median destructive field (MDF) is plotted against the dispersion parameter (DP) of ARM acquisition curves (Figure 6.1). In this diagram, we can separate two major groups: biogenic and detrital (plus pedogenic) magnetite. Biogenic magnetite (soft and hard components) has MDF values higher than 30 mT and DP values below 0.28. Detrital magnetite (plus extracellular and pedogenic magnetite) has MDF values below 32.5 mT and DP values higher than 0.22. Figure 6.1 also includes results obtained from other stalagmite studies (Lascu & Feinberg, 2011; Osete et al., 2012; Font et al., 2014; Bourne et al., 2015) and those from sediments collected inside and outside the Pau d'Alho cave. All stalagmite results plot together with the detrital group, except for a handful of data points reported by Lascu & Feinberg (2011), who used unmixing to demonstrate contributions from both pedogenic and loess sources. The data from Alho 6 form a tight cluster and overlap the field of detrital (plus pedogenic or extracellular) magnetite. Sediments related to the cave also plot together with the stalagmite data. So far, the data available for all stalagmites define distinct clusters in the diagram and suggest that these parameters can be used as fingerprints of specific processes of magnetic mineral assembly formation for each cave system (Figure 6.1). The similarity between magnetic properties of pedogenic and extracellular magnetite suggests a common origin for them, possibly related to bacterial dissimilatory iron reduction (Egli, 2004). The magnetic particles reaching the Alho 6 stalagmite are likely to have been formed during soil development. A similar pedogenic

derivation can be tentatively attributed to goethite. This mineral seems to be pervasive in soils and sediments (e.g. Till et al. 2014; Maxbauer et al. 2016) and also in stalagmites (e.g. Perkins, 1996; Lascu & Feinberg, 2011; Strauss et al., 2013). The fact that goethite and magnetite are present always in similar proportion in our samples, in spite of variations in the total concentration of magnetic minerals throughout the stalagmite suggests a common origin for both minerals. However, goethite may also form during speleogenesis, because dissolved iron in groundwater re-equilibrates with the Eh-pH conditions of the cave system at a speleothem drip point (Strauss et al., 2013).

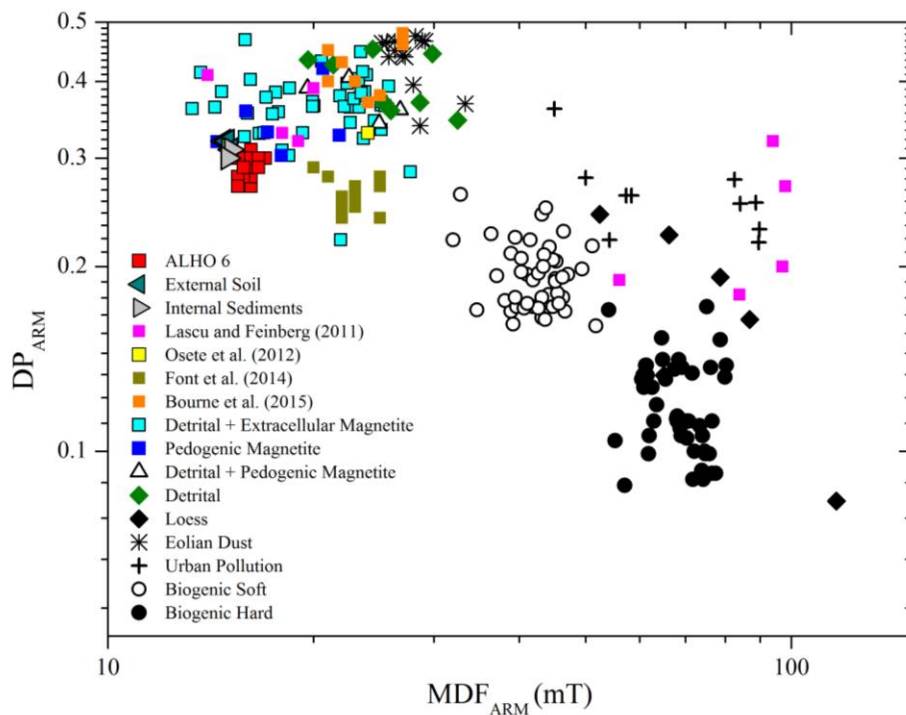


Figure 6.1: Anhysteretic Remanence Magnetization (ARM) parameters after cumulative log-Gaussian function (CLG) adjustment, (DP: dispersion parameter, MDF: median destructive field) for magnetite and maghemite in different environments (Egli, 2004) and results for other stalagmites (Lascu & Feinberg, 2011, Osete et al., 2012, Font et al., 2014, Bourne et al.2015. Red squares, dark green left-pointing triangle and grey right-pointing triangle indicate results from this study.

6.2 Variation in the magnetic signal and paleoclimatic significance

The results provide support for a relationship between isotopic and magnetic signals of the Alho 6 speleothem across decadal to centennial time scales. In general, more negative (positive) carbon and oxygen isotope ratios correspond to lower (higher) values in all magnetic remanence measurements. To simplify the visualization only the parameters ARM and HIRM are plotted with the isotope records and the growth rate in Figure 6.2. It is clear in the figure that the dry period MCA is characterized by elevated $\delta^{18}\text{O}$ and $\delta^{13}\text{C}$ values and higher magnetizations. Conversely, the wet period LIA shows generally lower $\delta^{18}\text{O}$ and $\delta^{13}\text{C}$ values and weaker magnetizations. The peaks in magnetization at 725 ± 18 CE, 802 ± 18 CE, 838 ± 21 CE and 888 ± 21 CE, correlate with peaks in the isotopic data. For the 1480-1600 CE interval, this relation is valid for $\delta^{13}\text{C}$ values, but does not hold for $\delta^{18}\text{O}$. This correlation between drier environmental conditions and elevated concentrations of magnetic minerals runs contrary to conventional thinking associated with the production of magnetite in soils, where a higher concentration of magnetic minerals would be expected in the humid periods not in the drier ones.

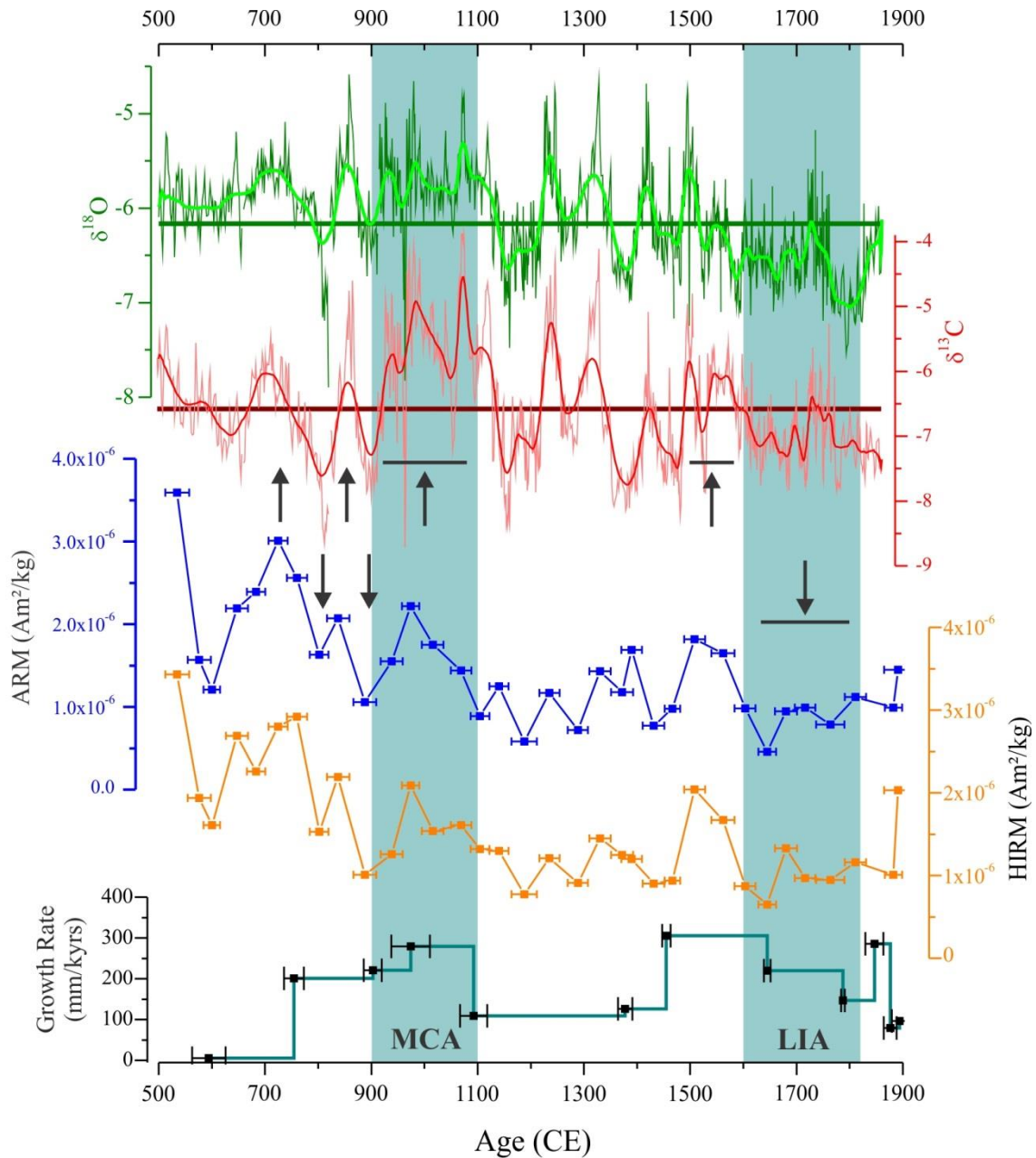


Figure 6.2: Records obtained in Alho 6 stalagmite, green lines indicates oxygen isotope (with their respective average and moving average), red lines indicates carbon isotope (with their respective average and moving average), the black arrows indicates the relationship observed between the isotope records (oxygen and carbon records) with the magnetic records such as anhysteretic remanence magnetization (ARM), blue lines, and “hard” isothermal remanence magnetization (HIRM), orange lines, and the growth rate of the stalagmite based on U-Th dating. Blue shades indicate the Medieval Climate Anomaly (MCA) and the Little Ice Age (LIA) respectively.

Earlier studies have proposed a link between the concentration of pedogenic magnetite and local precipitation rates in soils and speleothems (e.g. Bourne et al., 2015; Maher, 1998; Maxbauer et al., 2016). However, while the rate of magnetite production in soils has been shown to vary with precipitation, it is unclear whether elevated concentrations of magnetite in speleothems are a result of increased pedogenic activity (e.g., Bourne et al., 2015), or due to the changes in the rate of downward translocation of micrometer scale minerals during periods of increased precipitation (Maher and Taylor, 1988), or a combination of the two. As in Bourne et al. (2015), we are able to discuss the main environmental factors controlling the incorporation of detrital magnetic minerals into Alho 6 speleothem by comparing the magnetic data with stable carbon and oxygen isotope ratios measured on the same samples. This study is unique in that we examine these relationships on far shorter timescales than previously possible (e.g. Bourne et al., 2015).

The magnetization record in Alho 6 shows an inverse correlation with precipitation rate as determined by $\delta^{18}\text{O}$ values (Figure 6.2). This suggests that fine scale variations in the concentration of magnetite and goethite are not necessarily driven by increased rainfall in the study area. On the contrary, higher concentrations of magnetic minerals correspond to relative drier periods as inferred from the more positive $\delta^{18}\text{O}$ values observed in Alho 6. Thus, a higher flux of groundwater through overlying soil is not the main factor controlling magnetic mineral delivery to the speleothem of Pau d'Alho cave.

Further insights can be provided by examining the relationship between the $\delta^{13}\text{C}$ record and magnetic remanence in Alho 6. The carbon isotope value recorded by a speleothem is controlled by processes occurring in the soil/epikarst and inside the cave (Fairchild & Baker, 2012; Wong & Breecker, 2015). Changes in $\delta^{13}\text{C}$ in soils of tropical Brazil are usually driven by changes in the relative contributions of C_3 and C_4 plants to the carbon isotope composition of the soil organic matter (SOM) (e.g. Silva et al.; 2008, Pessenda et al., 2010). During wetter intervals, as denser forests (C_3 plants) replace savanna grasslands (C_4 plants), the soils displays a decrease in the $\delta^{13}\text{C}$ of the SOM. The increase in soil biomass during forest expansion is also likely to generate a higher concentration of isotopically lighter biogenic carbon, regardless of the relative ratio of C_3 and C_4 plants (Baldini et al., 2005). Consequently, it is possible that the carbon isotope composition recorded by the Alho 6 speleothem moves towards more negative values during times of

forest expansion, in agreement with the generally more negative values of $\delta^{18}\text{O}$ that usually covary with decreases in $\delta^{13}\text{C}$. On the timescales studied here, we suggest that the increased soil biomass associated with the formation of denser vegetation retains pedogenic magnetic minerals more effectively than grassland soils, leading to a reduced flux of magnetite into the underlying karst system.

While the $\delta^{13}\text{C}$ values in the Alho 6 record (ranging between -5 to -8 ‰) indicate that carbon from SOM played an important role, other fractionation processes are likely to have contributed to the $\delta^{13}\text{C}$ record as well; especially those processes that occur inside the cave or in the unsaturated aquifer above the cave system. For example, seasonal variations in cave venting can change the rate of CO_2 degassing that occurs during speleothem formation (Boch et al., 2011; Breitenbach et al., 2015; Meyer et al., 2014; Spötl et al., 2005). This is particularly effective at caves situated in temperate climates, which are characterized by large temperature gradients between the cave's interior and the external environment, as well as by high summer soil CO_2 productivity. Studies of modern speleothems show that when precipitation of CaCO_3 occurs in cave atmospheres depleted in ^{13}C , speleothems record higher $\delta^{13}\text{C}$ values. The opposite is true when carbonate precipitation occurs in cave atmospheres enriched in ^{13}C . Thus, for temperate climates, periods of higher and lower $\delta^{13}\text{C}$ values are associated with cold winters and warm summers, respectively (Meyer et al., 2014).

Large fluctuations in cave CO_2 are observed at our tropical site, which often experiences higher CO_2 levels in cave air during wet and slightly warmer summer months. One way to test if the climate conditions inside the cave exerted a dominant control on the $\delta^{13}\text{C}$ of Alho 6 speleothem is by making a comparison with its growth rates (GR), because $\delta^{13}\text{C}$ and GR are both thought to be affected by seasonal fluctuations in cave $p\text{CO}_2$ (Banner, Guilfoyle, James, Stern, & Musgrove, 2007; Baldini, 2010). In most caves, the soil zone is the main source of CO_2 , which enters directly through fractures or from degassing of cave drip waters. At our study site, periods of elevated CO_2 in the soil and the cave are likely to occur during episodes of increased rainfall and warmer temperatures. Because this process could result in high $p\text{CO}_2$ levels in the cave, it may inhibit the average speleothem growth rate and also laminae thickness (Boch et al., 2011; Banner, Guilfoyle, James, Stern, & Musgrove, 2007; Baldini, 2010). While it is important to consider these mechanisms here,

it is important to note the lack of a relationship between $\delta^{13}\text{C}$ and GR in Alho 6. In fact, this speleothem shows similar values of GR during periods of anomalously high and low $\delta^{13}\text{C}$ values during MCA and LIA events (Figure 6.2), suggesting that progressive CO_2 degassing during carbonate precipitation in the cave and possibly in the vadose zone is not likely to exert a major control on the $\delta^{13}\text{C}$ of Alho 6, at least on multidecadal to centennial time scales. In this light, the close correspondence between $\delta^{13}\text{C}$ and the concentration of magnetic minerals supports the idea that carbon isotope variability is mainly associated with the production of biogenic carbon in soil, where the decreased flux of magnetic minerals into Alho 6 at periods of higher rainfall (as denoted by low $\delta^{18}\text{O}$ values) is by explained by the greater retentivity of magnetic minerals by soils with denser vegetative cover. This notion is consistent with the lower $\delta^{13}\text{C}$ values expected to occur in soils during warmer and wetter periods with high biogenic CO_2 production. Thus on multidecadal to centennial time-scales, while $\delta^{18}\text{O}$ values track the variability of regional precipitation patterns near Pau d'Alho cave, we suggest that the records of $\delta^{13}\text{C}$ and mineral magnetism capture short term soil dynamics. A scheme of the soil dynamics in a karst system summarizing the results found here is presented in figure 6.3 (dry periods) and in figure 6.4 (wet periods).

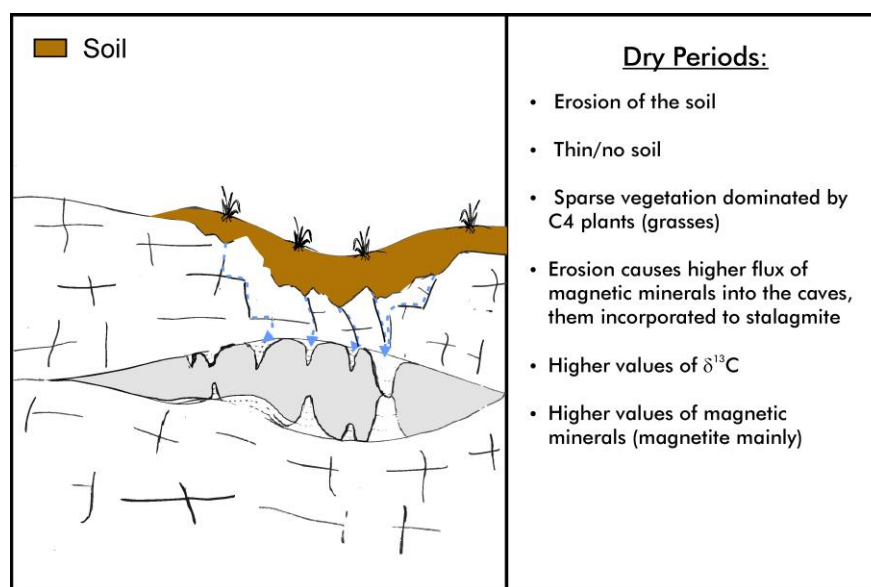


Figure 6.3: Scheme summarizing the soil dynamics found with the magnetic minerals for dry periods.

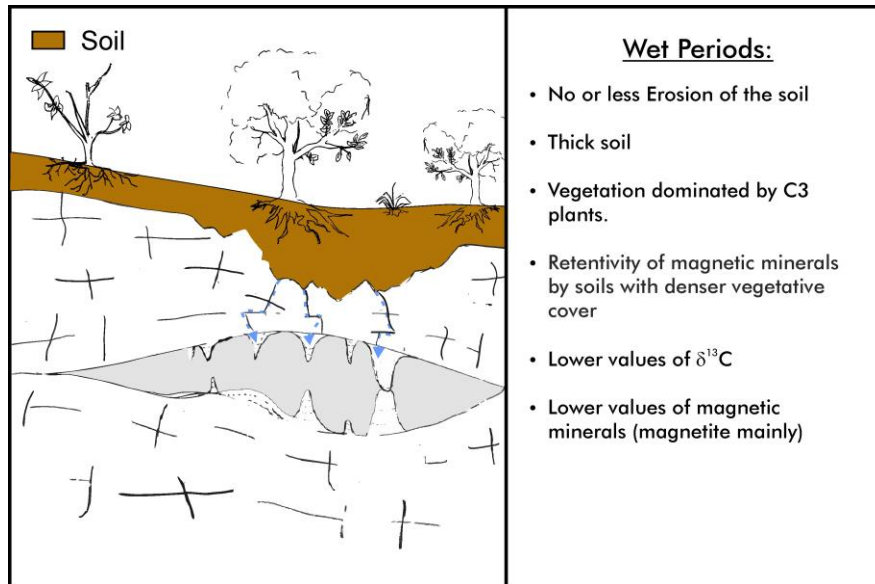


Figure 6.4: Scheme summarizing the soil dynamics found with the magnetic minerals for wet periods.

Chapter 7: Conclusion and Perspectives

The magnetic mineral assembly in stalagmite Alho 6 consists of fine-grained magnetite and goethite in a nearly constant proportion along the whole speleothem. The magnetic properties of the soft-coercivity phase show very little variability across the entire stalagmite and are essentially identical to those of pedogenic magnetite. In line with recent work showing that goethite is a pervasive phase in soils and stalagmites, we suggest that goethite in Alho 6 is pedogenic as well, but cannot rule out the possibility of goethite nucleation and growth during speleogenesis. The variations in the concentration of these magnetic minerals can be used as a proxy for the flux of suspended material delivered to the Pau d'Alho cave system via drip waters.

We conclude that the combined variability of magnetic parameters, $\delta^{13}\text{C}$ and $\delta^{18}\text{O}$ in the Alho 6 speleothem can provide new insights into the processes controlling the soil production in tropical regions. Our results indicate that a soil's retentiveness of its magnetic minerals is more strongly influenced by variations in vegetation cover than by changes in the rate of precipitation on multidecadal to centennial timescales of the last millennium in Midwest Brazil. The data suggest that the expansion of dense vegetation during wet periods might reduce the downward translocation of micrometer-scale pedogenic minerals from soils, resulting in speleothems characterized by low concentrations of magnetic minerals and low $\delta^{13}\text{C}$ values.

This study offers a new perspective for speleothem researchers on how environmental magnetic techniques may be combined with stable isotope methods to arrive at a more nuanced paleoclimate reconstruction that accounts for short-term variability in soil dynamics.

References

- Baldini, J. U. (2010). Cave atmosphere controls on stalagmite growth rate and palaeoclimate records. Geological Society, London, Special Publications, 336(1), 283-294.
- Baldini, J. U. L., McDermott, F., Baker, A., Baldini, L. M., Matthey, D. P., & Railsback, L. B. (2005). Biomass effects on stalagmite growth and isotope ratios: A 20th century analogue from Wiltshire, England. *Earth and Planetary Science Letters*, 240(2), 486–494. <http://doi.org/10.1016/j.epsl.2005.09.022>
- Banner, J. L., Guilfoyle, A., James, E. W., Stern, L. a., & Musgrove, M. (2007). Seasonal Variations in Modern Speleothem Calcite Growth in Central Texas, U.S.A. *Journal of Sedimentary Research*, 77(8), 615–622. <http://doi.org/10.2110/jsr.2007.065>
- Boch, R., Spötl, C., & Frisia, S. (2011). Origin and palaeoenvironmental significance of lamination in stalagmites from Katerloch Cave, Austria. *Sedimentology*, 58(2), 508–531. <http://doi.org/10.1111/j.1365-3091.2010.01173.x>
- Bourne, M. D., Feinberg, J. M., Strauss, B. E., Hardt, B., Cheng, H., Rowe, H. D., Edwards, R. (2015). Long-term changes in precipitation recorded by magnetic minerals in speleothems. *Geology*, 43(7), 595–598. <http://doi.org/10.1130/G36695.1>
- Breitenbach, S. F. M., Lechleitner, F. A., Meyer, H., Diengdoh, G., Matthey, D., & Marwan, N. (2015). Cave ventilation and rainfall signals in dripwater in a monsoonal setting - a monitoring study from NE India. *Chemical Geology*, 402, 111–124. <http://doi.org/10.1016/j.chemgeo.2015.03.011>
- Butler, R. F. (1992). Paleomagnetism: magnetic domains to geologic terranes (Vol. 319). *Boston: Blackwell Scientific Publications*.
- Cheng, H., Lawrence Edwards, R., Shen, C. C., Polyak, V. J., Asmerom, Y., Woodhead, J., ... Calvin Alexander, E. (2013). Improvements in ²³⁰Th dating, ²³⁰Th and ²³⁴U half-life values, and U-Th isotopic measurements by multi-collector inductively coupled plasma mass spectrometry. *Earth and Planetary Science Letters*, 371-372, 82–91. <http://doi.org/10.1016/j.epsl.2013.04.006>
- Cisowski, S. (1981). Interacting vs. non-interacting single domain behavior in natural and synthetic samples. *Physics of the Earth and Planetary Interiors*, 26(1-2), 56–62. [http://doi.org/10.1016/0031-9201\(81\)90097-2](http://doi.org/10.1016/0031-9201(81)90097-2)
- Collinson, D. W. (1983). *Methods in palaeomagnetism and rock magnetism*.
- Cornell, R. M., & Schwertmann, U. (2001). *The Iron Oxides. Structure, Properties*.
- Cruz, F. W., Burns, S. J., Karmann, I., Sharp, W. D., Vuille, M., Cardoso, A. O., ... & Viana, O. (2005). Insolation-driven changes in atmospheric circulation over the past 116,000 years in subtropical Brazil. *Nature*, 434(7029), 63-66. Cruz, F.W. et al., 2006. A stalagmite record of changes in atmospheric circulation and soil processes in the Brazilian subtropics during the Late Pleistocene. *Quaternary Science Reviews*, 25(21-22), pp.2749–2761.
- Cruz, F. W., Burns, S. J., Karmann, I., Sharp, W. D., Vuille, M., & Ferrari, J. A. (2006). A stalagmite record of changes in atmospheric circulation and soil processes in the Brazilian

- subtropics during the Late Pleistocene. *Quaternary Science Reviews*, 25(21-22), 2749–2761. <http://doi.org/10.1016/j.quascirev.2006.02.019>
- Dunlop and Özden Özdemir., D. J. (1997). Rock Magnetism. Retrieved from <http://dx.doi.org/10.1017/CBO9780511612794>
- Dunlop, D. J. (2002). Theory and application of the Day plot (Mrs/Ms versus Hcr/Hc) 2. Application to data for rocks, sediments, and soils. *Journal of Geophysical Research*, 107(B3), 1–15. <http://doi.org/10.1029/2001JB000487>
- Egli, R. (2004). Characterization of individual rock magnetic components by analysis of remanence curves, 1. Unmixing natural sediments. *Studia Geophysica et Geodaetica*, 48(2), 391–446. <http://doi.org/10.1023/B:SGEG.0000020839.45304.6d>
- Evans, M., & Heller, F. (2003). Environmental magnetism: principles and applications of enviromagnetics (Vol. 86). *Academic press*.
- Fairchild, I. J., & Baker, A. (2012). *Science From Process to Past Environments*.
- Fairchild, I. J., Smith, C. L., Baker, A., Fuller, L., Spötl, C., Matthey, D., & McDermott, F. (2006). Modification and preservation of environmental signals in speleothems. *Earth-Science Reviews*, 75(1), 105-153.
- Fairchild, I. J., Smith, C. L., Baker, A., Fuller, L., Spötl, C., Matthey, D., & McDermott, F. (2006). Modification and preservation of environmental signals in speleothems. *Earth-Science Reviews*, 75(1-4), 105–153. <http://doi.org/10.1016/j.earscirev.2005.08.003>
- Font, E., Veiga-Pires, C., Pozo, M., Carvallo, C., Carlos de Siqueira Neto, A., Camps, P., ... Mirão, J. (2014). Journal of Geophysical Research : Solid Earth. *Journal of Geophysical Research: Solid Earth*, 119, 1–28. <http://doi.org/10.1002/2014JB011381>.Received
- Gornitz, V. (Ed.). (2008). *Encyclopedia of paleoclimatology and ancient environments*. Springer Science & Business Media.
- Guyodo, Y., LaPara, T. M., Anschutz, A. J., Penn, R. L., Banerjee, S. K., Geiss, C. E., & Zanner, W. (2006). Rock magnetic, chemical and bacterial community analysis of a modern soil from Nebraska. *Earth and Planetary Science Letters*, 251(1-2), 168–178. <http://doi.org/10.1016/j.epsl.2006.09.005>
- Harrison, R. J., & Feinberg, J. M. (2008). FORCinel: An improved algorithm for calculating first-order reversal curve distributions using locally weighted regression smoothing. *Geochemistry, Geophysics, Geosystems*, 9(5). <http://doi.org/10.1029/2008GC001987>
- Heslop, D. (2015). Numerical strategies for magnetic mineral unmixing. *Earth-Science Reviews*, 150, 256–284. <http://doi.org/10.1016/j.earscirev.2015.07.007>
- Heslop, D., & Roberts, A. P. (2012). Estimation of significance levels and confidence intervals for first-order reversal curve distributions. *Geochemistry, Geophysics, Geosystems*, 13(12). <http://doi.org/10.1029/2012GC004115>
- Jackson, M., Bowles, J. A., Lascu, I., & Solheid, P. (2010). Deconvolution of u channel magnetometer data: Experimental study of accuracy, resolution, and stability of different inversion methods. *Geochemistry, Geophysics, Geosystems*, 11(7), 1–21. <http://doi.org/10.1029/2009GC002991>

- Jackson, M., Worm, H. U., & Banerjee, S. K. (1990). Fourier analysis of digital hysteresis data: rock magnetic applications. *Physics of the Earth and Planetary Interiors*, 65(1-2), 78–87. [http://doi.org/10.1016/0031-9201\(90\)90077-B](http://doi.org/10.1016/0031-9201(90)90077-B)
- Kirschvink, J. L. (1992). Uniform magnetic fields and double-wrapped coil systems: improved techniques for the design of bioelectromagnetic experiments. *Bioelectromagnetics*, 13(5), 401-411.
- Kirschvink, J. L., Isozaki, Y., Shibuya, H., Otofujii, Y. ichiro, Raub, T. D., Hilburn, I. A., Bonifacie, M. (2015). Challenging the sensitivity limits of Paleomagnetism: Magnetostratigraphy of weakly magnetized Guadalupian-Lopingian (Permian) Limestone from Kyushu, Japan. *Palaeogeography, Palaeoclimatology, Palaeoecology*, 418, 75–89. <http://doi.org/10.1016/j.palaeo.2014.10.037>
- Klimchouk, A. B., & Ford, D. C. (2000). Types of karst and evolution of hydrogeologic settings. *Speleogenesis: Evolution of Karst Aquifers*, (MAY), 45–53.
- Kruiver, P. P., Dekkers, M. J., & Heslop, D. (2001). Quantification of magnetic coercivity components by the analysis of acquisition curves of isothermal remanent magnetisation. *Earth and Planetary Science Letters*, 189(3-4), 269–276. [http://doi.org/10.1016/S0012-821X\(01\)00367-3](http://doi.org/10.1016/S0012-821X(01)00367-3)
- Lachniet, M. S. (2009). Climatic and environmental controls on speleothem oxygen-isotope values. *Quaternary Science Reviews*, 28(5-6), 412–432. <http://doi.org/10.1016/j.quascirev.2008.10.021>
- Lascu, I., & Feinberg, J. M. (2011). Speleothem magnetism. *Quaternary Science Reviews*, 30(23-24), 3306–3320. <http://doi.org/10.1016/j.quascirev.2011.08.004>
- Lascu, I., Feinberg, J. M., Dorale, J. A., Cheng, H., & Edwards, R. L. (2016). Age of the Laschamp excursion determined by U-Th dating of a speleothem geomagnetic record from North America. *Geology*, 44(2), 139–142. <http://doi.org/10.1130/G37490.1>
- Latham, A. G. (1981). Paleomagnetism, rock magnetism and U-Th dating of speleothem deposits, 534.
- Latham, A. G., Ford, D. C., Schwarcz, H. P., & Birchall, T. (1989). Secular variation from Mexican stalagmites: their potential and problems. *Physics of the Earth and Planetary Interiors*, 56(1-2), 34–48. [http://doi.org/10.1016/0031-9201\(89\)90034-4](http://doi.org/10.1016/0031-9201(89)90034-4)
- Latham, A. G., Schwarcz, H. P., Ford, D. C., & Pearce, G. W. (1979). Palaeomagnetism of stalagmite deposits. *Nature*. <http://doi.org/10.1038/280383a0>
- Liu, Q., Roberts, A. P., Larrasoana, J. C., Banerjee, S. K., Guyodo, Y., Tauxe, L., & Oldfield, F. (2012). Environmental Magnetism: Principles and Applications, 1–50. <http://doi.org/10.1029/2012RG000393>.
- Lowrie, W. (1990). Identification of ferromagnetic minerals in a rock by coercivity and unblocking temperature properties. *Geophys. Res. Lett.* 17, 159–162.
- Maher, B. A., & Thompson, R. (1992). Paleoclimatic significance of the mineral magnetic record of the Chinese loess and paleosols. *Quaternary Research*, 37(2), 155-170.
- Maher, B. A. (2007). Environmental magnetism and climate change. *Contemporary Physics*, 48(5),

247–274. <http://doi.org/10.1080/00107510801889726>

- Martin, K. (1990). Paleomagnetism of Speleothems in Gardner Cave, Washington. *National Speleological Society Bulletin*, 52, 87–94.
- Maxbauer, D. P., Feinberg, J. M., & Fox, D. L. (2016). Magnetic mineral assemblages in soils and paleosols as the basis for paleoprecipitation proxies: A review of magnetic methods and challenges. *Earth Science Reviews*, 155, 28–48. <http://doi.org/10.1016/j.epsl.2013.03.034>
- Meyer, K. W., Feng, W., Breecker, D. O., Banner, J. L., & Guilfoyle, A. (2014). Interpretation of speleothem calcite $\delta^{13}\text{C}$ variations: Evidence from monitoring soil CO_2 , drip water, and modern speleothem calcite in central Texas. *Geochimica et Cosmochimica Acta*, 142, 281–298. <http://doi.org/10.1016/j.gca.2014.07.027>
- Morinaga, H. (1989). Palaeomagnetism of stalagmites (speleothems) in S V V Japan Hiroo Inokuchi and Katsumi Yaskawa, 519–528.
- Morinaga, H., Horie, I., & Yaskawa, K. (1992). A geomagnetic reversal recorded in a stalagmite collected in western Japan. *J. Geomag. Geoelectr.*, 44, 661–675. <http://doi.org/10.5636/jgg.44.661>
- Morinaga, H., Inokuchi, H., & Yaskawa, K. (1986). Magnetization of a stalagmite in Akiyoshi Plateau as a record of the geomagnetic secular variation in West Japan. *J. Geomag. Geoelectr.*, 38, 27–44. <http://doi.org/10.5636/jgg.38.27>
- Novello, V. F., Vuille, M., Cruz, F. W., Strikis, N. M., de Paula, M. S., Edwards, R. L., ... Moquet, J. S. (2016). Centennial-scale solar forcing of the South American Monsoon System recorded in stalagmites. *Scientific Reports*, 6(April), 1–8. <http://doi.org/10.1038/srep24762>
- Openshaw, S., Latham, A., & Shaw, J. (1997). Speleothem palaeosecular variation records from China: Their contribution to the coverage of Holocene palaeosecular variation data in East Asia. *Journal of geomagnetism and geoelectricity*, 49(4), 485-505.
- Osete, M. L., Martin-Chivelet, J., Rossi, C., Edwards, R. L., Egli, R., Muñoz-Garcia, M. B., Heller, F. (2012). The Blake geomagnetic excursion recorded in a radiometrically dated speleothem. *Earth and Planetary Science Letters*, 353-354, 173–181. <http://doi.org/10.1016/j.epsl.2012.07.041>
- Özdemir, Ö., & Dunlop, D. J. (2014). Hysteresis and coercivity of hematite. *Journal of Geophysical Research: Solid Earth*, 119(4), 2582-2594.
- Perkins, A.M., Maher, B.A., 1993. Rock magnetic and palaeomagnetic studies of British speleothems. *Journal of Geomagnetism and Geoelectricity* 45, 143-153
- Perkins, A. M. (1996). Observations under electron microscopy of magnetic minerals extracted from speleothems. *Earth Planet. Sci. Let.*, 139(96), 281–289. [http://doi.org/10.1016/0012-821X\(96\)00013-1](http://doi.org/10.1016/0012-821X(96)00013-1)
- Pessenda, L. C. R., Gouveia, S. E. M., Ribeiro, A. de S., De Oliveira, P. E., & Aravena, R. (2010). Late Pleistocene and Holocene vegetation changes in northeastern Brazil determined from carbon isotopes and charcoal records in soils. *Palaeogeography, Palaeoclimatology, Palaeoecology*, 297(3-4), 597–608. <http://doi.org/10.1016/j.palaeo.2010.09.008>
- Pike, C. R., Roberts, A. P., & Verosub, K. L. (1999). Characterizing interactions in fine magnetic

- particle systems using first order reversal curves. *J. Appl. Phys.*, 85(9), 6660–6667.
<http://doi.org/10.1063/1.370176>
- Roberts, a. P., Pike, C. R., & Verosub, K. L. (2000). First-order reversal curve diagrams: a new tool for characterizing the magnetic properties of natural samples. *Journal of Geophysical Research*, 105(B12), 28461–475. <http://doi.org/10.1029/2000JB900326>
- Roberts, A. P., Heslop, D., Zhao, X., & Pike, C. R. (2014). Understanding fine magnetic particle systems through use of first-order reversal curve diagrams. *Reviews of Geophysics*, 52(4), 557-602.
- Robertson, D. J., & France, D. E. (1994). Discrimination of remanence-carrying minerals in mixtures, using isothermal remanent magnetisation acquisition curves. *Physics of the Earth and Planetary Interiors*, 82(3-4), 223–234. [http://doi.org/10.1016/0031-9201\(94\)90074-4](http://doi.org/10.1016/0031-9201(94)90074-4)
- Ruddiman. (2001). Earth ' s Climate System Today. *Earth ' s Climate: Past and Future*, 8.
- Spötl, C., Fairchild, I. J., & Tooth, A. F. (2005). Cave air control on dripwater geochemistry, Obir Caves (Austria): Implications for speleothem deposition in dynamically ventilated caves. *Geochimica et Cosmochimica Acta*, 69(10), 2451–2468.
<http://doi.org/10.1016/j.gca.2004.12.009>
- Silva, L. C., Sternberg, L., Haridasan, M., Hoffmann, W. A., Miralles-Wilhem, F., & Franco, A. C. (2008). Expansion of gallery forests into central Brazilian savannas. *Global Change Biology*, 14(9), 2108-2118.
- Strauss, B. E., Strehlau, J. H., Lascu, I., Dorale, J. A., Penn, R. L., & Feinberg, J. M. (2013). The origin of magnetic remanence in stalagmites: Observations from electron microscopy and rock magnetism. *Geochemistry, Geophysics, Geosystems*, 14(12), 5006–5025.
<http://doi.org/10.1002/2013GC004950>
- Strehlau, J. H., Hegner, L. A., Strauss, B. E., Feinberg, J. M., & Penn, R. L. (2014). Simple and efficient separation of magnetic minerals from speleothems and other carbonates. *Journal of Sedimentary Research*, 84(11), 1096–1106. <http://doi.org/10.2110/jsr.2014.89>
- Tauxe, L., Mullender, T. a. T., & Pick, T. (1996). Potbellies, wasp-waists, and superparamagnetism in magnetic hysteresis. *Journal of Geophysical Research*, 101(B1), 571.
<http://doi.org/10.1029/95JB03041>
- Till, J. L., Guyodo, Y., Lagroix, F., Morin, G., & Ona-Nguema, G. (2014). Goethite as a potential source of magnetic nanoparticles in sediments. *Geology*, 43(1), 75–78.
<http://doi.org/10.1130/G36186.1>
- Vuille, M., Burns, S. J., Taylor, B. L., Cruz, F. W., Bird, B. W., Abbott, M. B., ... Novello, V. F. (2012). A review of the South American monsoon history as recorded in stable isotopic proxies over the past two millennia. *Climate of the Past*, 8(4), 1309–1321.
<http://doi.org/10.5194/cp-8-1309-2012>
- Wong, C. I., & Breecker, D. O. (2015). Advancements in the use of speleothems as climate archives. *Quaternary Science Reviews*, 127, 1–18.
<http://doi.org/10.1016/j.quascirev.2015.07.019>
- Xie, S., Evershed, R. P., Huang, X., Zhu, Z., Pancost, R. D., Meyers, P. A., ... Zhu, J. (2013). Concordant monsoon-driven postglacial hydrological changes in peat and stalagmite records

and their impacts on prehistoric cultures in central China. *Geology*, 41(8), 827–830.
<http://doi.org/10.1130/G34318.1>

Zhu, Z., Zhang, S., Tang, C., Li, H., Xie, S., Ji, J., & Xiao, G. (2012). Magnetic fabric of stalagmites and its formation mechanism. *Geochemistry, Geophysics, Geosystems*, 13(6), 1–12. <http://doi.org/10.1029/2011GC003869>

Appendix 1

(Rock Magnetism results)

Table 1: Rock magnetism results from Alho 6 stalagmite, where NRM: Natural Remanence Magnetization; ARM: Anhysteretic Remanence magnetization; SIRM: Saturation Isothermal Remanence; HIRM: Hard coercivity Isothermal Remanence Magnetization; Soft IRM: Soft coercivity Isothermal Remanence Magnetization.

| Sample # | Depth (mm) | Thickness (mm) | Age (CE) | Average age | Mass (kg) | NRM (Am ² /kg) | ARM (Am ² /kg) | SIRM (Am ² /kg) | HIRM (Am ² /kg) | Soft IRM (Am ² /kg) | S-ratio |
|----------|------------|----------------|----------|-------------|-----------|---------------------------|---------------------------|----------------------------|----------------------------|--------------------------------|---------|
| 1 | 5 | 9.0 | 1891 | 53.4 | 0.004911 | 1.40E-05 | 1.45E-04 | 3.38E-03 | 2.03E-04 | 3.18E-03 | 0.88 |
| 2 | 6 | 5.5 | 1882 | 32.6 | 0.003768 | 2.17E-05 | 9.93E-05 | 2.22E-03 | 1.01E-04 | 2.12E-03 | 0.91 |
| 3 | 18 | 6.7 | 1811 | 39.8 | 0.004955 | 2.40E-05 | 1.12E-04 | 2.28E-03 | 1.16E-04 | 2.16E-03 | 0.90 |
| 4 | 26 | 9.0 | 1764 | 53.4 | 0.006322 | 1.90E-05 | 7.85E-05 | 1.90E-03 | 9.47E-05 | 1.80E-03 | 0.90 |
| 5 | 34 | 6.6 | 1716 | 39.2 | 0.004422 | 3.01E-05 | 9.91E-05 | 2.15E-03 | 9.70E-05 | 2.05E-03 | 0.91 |
| 6 | 40 | 7.0 | 1680 | 41.6 | 0.004912 | 1.72E-05 | 9.47E-05 | 2.10E-03 | 1.33E-04 | 1.97E-03 | 0.87 |
| 7 | 46 | 5.6 | 1645 | 33.2 | 0.003968 | 1.16E-05 | 4.56E-05 | 1.23E-03 | 6.49E-05 | 1.16E-03 | 0.89 |
| 8 | 53 | 6.6 | 1603 | 39.2 | 0.004941 | 5.36E-05 | 9.84E-05 | 2.07E-03 | 8.73E-05 | 1.99E-03 | 0.92 |
| 9 | 60 | 7.3 | 1562 | 43.4 | 0.005248 | 5.72E-05 | 1.65E-04 | 3.40E-03 | 1.67E-04 | 3.23E-03 | 0.90 |
| 10 | 69 | 6.6 | 1508 | 39.2 | 0.004891 | 6.40E-05 | 1.82E-04 | 3.74E-03 | 2.04E-04 | 3.53E-03 | 0.89 |
| 11 | 76 | 4.9 | 1467 | 29 | 0.003474 | 2.94E-05 | 9.78E-05 | 2.04E-03 | 9.40E-05 | 1.94E-03 | 0.91 |
| 12 | 82 | 6.9 | 1431 | 41 | 0.005049 | 3.27E-05 | 7.72E-05 | 1.68E-03 | 9.03E-05 | 1.59E-03 | 0.89 |
| 13 | 89 | 6.5 | 1390 | 38.6 | 0.004372 | 6.27E-05 | 1.69E-04 | 3.18E-03 | 1.20E-04 | 3.06E-03 | 0.92 |
| 14 | 92 | 7.0 | 1372 | 41.6 | 0.004913 | 4.80E-05 | 1.18E-04 | 2.41E-03 | 1.25E-04 | 2.28E-03 | 0.90 |
| 15 | 99 | 6.8 | 1330 | 40.4 | 0.004951 | 6.18E-05 | 1.43E-04 | 2.92E-03 | 1.45E-04 | 2.78E-03 | 0.90 |
| 16 | 106 | 6.4 | 1289 | 38 | 0.004522 | 3.54E-05 | 7.22E-05 | 1.73E-03 | 9.09E-05 | 1.64E-03 | 0.90 |
| 17 | 115 | 6.4 | 1235 | 38 | 0.004567 | 3.37E-05 | 1.17E-04 | 2.21E-03 | 1.21E-04 | 2.09E-03 | 0.89 |
| 18 | 123 | 8.0 | 1188 | 47.4 | 0.005692 | 2.64E-05 | 5.84E-05 | 1.26E-03 | 7.74E-05 | 1.18E-03 | 0.88 |
| 19 | 131 | 6.0 | 1140 | 35.6 | 0.004302 | 4.65E-05 | 1.25E-04 | 2.41E-03 | 1.30E-04 | 2.28E-03 | 0.89 |
| 20 | 137 | 6.0 | 1105 | 35.6 | 0.004367 | 4.12E-05 | 8.90E-05 | 2.02E-03 | 1.32E-04 | 1.89E-03 | 0.87 |
| 21 | 143 | 6.5 | 1069 | 38.6 | 0.004748 | 7.29E-05 | 1.44E-04 | 2.82E-03 | 1.61E-04 | 2.66E-03 | 0.89 |
| 22 | 152 | 6.8 | 1016 | 40.4 | 0.005016 | 8.07E-05 | 1.75E-04 | 3.21E-03 | 1.54E-04 | 3.06E-03 | 0.90 |
| 23 | 159 | 5.4 | 974 | 32 | 0.003271 | 1.00E-04 | 2.22E-04 | 4.36E-03 | 2.09E-04 | 4.15E-03 | 0.90 |
| 24 | 165 | 7.0 | 938 | 41.6 | 0.005078 | 8.61E-05 | 1.55E-04 | 2.93E-03 | 1.26E-04 | 2.80E-03 | 0.91 |
| 25 | 174 | 7.2 | 888 | 42.8 | 0.004970 | 4.47E-05 | 1.06E-04 | 2.02E-03 | 1.01E-04 | 1.92E-03 | 0.90 |
| 26 | 182 | 7.1 | 837 | 42.2 | 0.005115 | 1.13E-04 | 2.07E-04 | 4.17E-03 | 2.19E-04 | 3.96E-03 | 0.90 |
| 27 | 188 | 6.0 | 802 | 35.6 | 0.004147 | 8.75E-05 | 1.63E-04 | 3.34E-03 | 1.53E-04 | 3.19E-03 | 0.91 |

| | | | | | | | | | | | |
|----------------|-----|------------|-----|-------------|-----------------|-----------------|-----------------|-----------------|-----------------|-----------------|-------------|
| 28 | 195 | 6.5 | 760 | 38.6 | 0.004477 | 1.05E-04 | 2.56E-04 | 5.45E-03 | 2.92E-04 | 5.16E-03 | 0.89 |
| 29 | 201 | 6.0 | 725 | 35.6 | 0.004233 | 1.53E-04 | 3.01E-04 | 5.96E-03 | 2.80E-04 | 5.68E-03 | 0.91 |
| 30 | 208 | 5.8 | 683 | 34.4 | 0.004108 | 1.28E-04 | 2.39E-04 | 4.94E-03 | 2.26E-04 | 4.72E-03 | 0.91 |
| 31 | 214 | 7.0 | 648 | 41.6 | 0.004610 | 9.78E-05 | 2.19E-04 | 4.49E-03 | 2.69E-04 | 4.22E-03 | 0.88 |
| 32 | 222 | 5.3 | 600 | 31.4 | 0.003403 | 5.79E-05 | 1.21E-04 | 2.80E-03 | 1.61E-04 | 2.64E-03 | 0.88 |
| 33 | 226 | 7.3 | 576 | 43.4 | 0.004872 | 7.45E-05 | 1.57E-04 | 3.50E-03 | 1.94E-04 | 3.30E-03 | 0.89 |
| 34 | 233 | 7.6 | 535 | 45.2 | 0.004934 | 1.38E-04 | 3.59E-04 | 7.19E-03 | 3.43E-04 | 6.85E-03 | 0.90 |
| Average | | 6.7 | | 39.5 | 0.004633 | 6.08E-05 | 1.47E-04 | 3.05E-03 | 1.55E-04 | 2.89E-03 | 0.90 |